Πανεπιστήμιο Δυτικής Μακεδονίας
Τμήμα Μηχανολόγων Μηχανικών

Διπλωματική εργασία

Αεροδυναμική Βελτιστοποίηση του Εμπρόσθιου Μέρους Ενός Μη Αεροδυναμικού Σώματος

ΙΩΑΝΝΗΣ ΜΠΟΥΡΑΣ
Α.Ε.Μ.: 300

Επιβλέπων Καθηγητής:
Δρ. Αντώνιος Τουρλιδάκης

ΚΟΖΑΝΗ 2013

Πανεπιστήμιο Δυτικής Μακεδονίας
Τμήμα Μηχανολόγων Μηχανικών

Διπλωματική Εργασία

Η παρούσα εργασία πραγματοποιήθηκε στα πλαίσια του Ευρωπαϊκού προγράμματος κινητικότητας ERASMUS και του μεταπτυχιακού προγράμματος MSc. In Computational Fluid Dynaimcs σε συνεργασία με το πανεπιστήμιο του Cranfield της Αγγλίας. Το πανεπιστήμιο του Cranfield διατηρεί τα πνευματικά δικαιώματα της παρούσας εργασίας, όπως αναφέρεται παρακάτω.

Αεροδυναμική Βελτιστοποίηση του Εμπρόσθιου Μέρους Ενός Μη Αεροδυναμικού Σώματος

Ιωάννης Μπούρας
Α.Ε.Μ.: 300

Επιβλέπων καθηγητής του Πανεπιστημίου Δυτικής Μακεδονίας:
Δρ. Αντώνιος Τουρλιδάκης

Επιβλέπων καθηγητής στο πανεπιστήμιο του Cranfield:
Dr. Laszlo Konozsy
Επιβλέπων βιομηχανίας:
Dr. Date Rentema

ΚΟΖΑΝΗ 2013

Πρόλογος

Η παρούσα διπλωματική εργασία ασχολείται με την αεροδυναμική βελτιστοποίηση του εμπρόσθιου μέρους ενός μη αεροδυναμικού σώματος. Η διπλωματική ξεκινάει με μια βιβλιογραφική επισκόπηση προηγούμενων συγγραφέων και μια εισαγωγή στην επιστήμη της υπολογιστικής ρευστομηχανικής και των μεθόδων της. 3 διαφορετικές εμπρόσθιες γεωμετρίες εξετάστηκαν. Η επαλήθευση πειραματικών δεδομένων σε παρόμοια σώματα ήταν επιτυχής για μηδενική γωνία πρόσκρουσης του αέρα με το σώμα για πλήρως προσκολλημένη και πλήρως αποκολλημένη ροή. Η πρώτη από τις 3 γεωμετρίες αναπαριστά ουσιαστικά ένα ορθογώνιο παραλληλεπίπεδο. Παρά την απλότητα της γεωμετρίας, τα αεροδυναμικά φαινόμενα που λαμβάνουν χώρα είναι εξαιρετικά ενδιαφέροντα καθώς η ροή είναι πλήρως αποκολλημένη και ισχυρές δίνες εμφανίζονται στην περιοχή απόρρους, ενώ η εμπρόσθια περιοχή κυριαρχείται από έντονες δυνάμεις πίεσης, αυξάνοντας σημαντικά τον αεροδυναμικό συντελεστή του σώματος. Το δεύτερο σώμα, το οποίο αναπαριστά στο περίπου ένα απλοϊκό φορτηγό αυτοκίνητο, παρουσιάζει μια πιο ομαλή ροή γύρω του και λιγότερο έντονες αποκολλήσεις φυσαλίδων αλλά εξ' αιτίας έντονων δυνάμεων πίεσης και κάποιων ανακυκλοφοριών λόγω της πιο περίπλοκης γεωμετρίας του εξακολουθεί να έχει αυξημένο συντελεστή πίεσης για φορτηγό αυτοκίνητο. Το τρίτο μοντέλο, που έχει μια ελλειπτική μορφή εμπρός του σώματος και η ροή είναι πλήρως προσκολλημένη για μεγάλους αριθμούς Reynolds τουλάχιστον που αντιστοιχούν σε κανονικές ταχύτητες για φορτηγά αυτοκίνητα, παρουσιάζει αρκετά χαμηλό αεροδυναμικό συντελεστή και είναι αρκετά υποσχόμενο για μελλοντική εξέλιξη.

CRANFIELD UNIVERSITY

Johnnie Bouras

Aerodynamic Optimization of the Front of a Blunt Body

School of Engineering

MSc in Computational Fluid Dynamics

MSc THESIS

Academic Year : 2012-2013

Supervisor: Dr. Laszlo Konozsy

Industrial Supervisor: Dr. Date Rentema

September 2013

CRANFIELD UNIVERSITY

School of Engineering

MSc in Computational Fluid Dynamics

MSc Thesis

Academic Year: 2012-2013

Johnnie Bouras

Aerodynamic optimization of the front of a Blunt body

Supervisor(s):

Dr. Laszlo Konozsy

Dr. Date Rentema

Except where acknowledged in the customary manner, the material presented in this thesis is, to the best of my knowledge, original and has not been submitted in whole or part for a degree in any university.

_____

Johnnie Bouras

Abstract

The present thesis deals with the shape optimization of the frontal area of blunt bodies. It starts with a literature review of previous authors and an introduction to the science of CFD and its methods. 3 different frontal shapes were simulated of a specific blunt body. Validation of experimental data was successful with similar geometries for no yaw angle for fully separated as well as for fully attached flows. The first model represents a rectangular box. Despite its simplicity the flow phenomena that occur around it are significant because the flow is fully separated and strong vortices occur around it and the frontal area is dominated by pressure forces, leading to an increased drag coefficient. The second model which represents roughly a real truck shows a more smooth flow around it with by far smaller in size bubble separations but due to some recirculations that occur at the front of it as it has a more complex geometry, as well as significant pressure forces at its frontal area, it has a significant drag coefficient. The last model has an elliptical frontal shape and the flow is fully attached for high Reynolds numbers which correspond to average velocities for real trucks, lead to a low drag coefficient and it is very promising for future work.

Acknowledgments

First of all, I would like to thank my supervisor during my studies in Cranfield university Mr. Lazlo Konozsy who spent countless hours with me having face to face discussions or telephone calls including weekends helping me with numerous difficulties that I encountered during these 3.5 months that my thesis lasted. I am also grateful to Mr. Nick Asproulis who was always willing to help anytime I needed him during the whole year. Also, I would like to express my deepest appreciation to Mr. Antonis Tourlidakis, my tutor during my undergraduate studies who was the one and only who believed in me and he suggested that I attend an MSc. program in Cranfield university. Many thanks also to my friend Vasilis, with whom we have numerous conversations and debates regarding CFD topics, as well as fun everytime we meet. Finally, I would like to thank personally Christine, my best friend, for her continuous support all these years, despite the fact that we live far away from each other.

Johnnie Bouras

Contents

List of Figures

List of Tables

Nomenclature

Roman symbols

A	Area (m^2)
D	Characteristic length (m)
C_v	Specific heat capacity at constant volume ($J/Kg \cdot K$)
$\vec{F}$	Force (N)
g	Acceleration of gravity (m/s^2)
i	Specific internal energy (J/Kg)
k	Turbulent kinetic energy (m^2/s^2)
P	Pressure (Pa)
r	Radius (m)
S_{Mx}	Momentum source in x direction (Kg/s^2m^2)
S_{My}	Momentum source in y direction (Kg/s^2m^2)
S_{Mz}	Momentum source in z direction (Kg/s^2m^2)
T	Temperature (K)
t	Time (s)
$\vec{u}$	Velocity vector (m/s)
u	Velocity magnitude in x direction (m/s)
$\bar{u}$	Averaged velocity in x direction in a period of time (m/s)
$u^{'}$	Velocity fluctuation in x direction in a period of time (m/s)

v	Velocity magnitude in y direction (m/s)
$\bar{v}$	Averaged velocity in y direction in a period of time (m/s)
$v^{'}$	Velocity fluctuation in y direction in a period of time (m/s)
w	Velocity magnitude in z direction (m/s)
$\bar{w}$	Averaged velocity in z direction in a period of time (m/s)
$w^{'}$	Velocity fluctuation in z direction in a period of time (m/s)
v_m	Mass averaged velocity (m/s)
v_{ref}	Reference velocity (m/s)
x,y,z	Cartesian coordinates

Greek symbols

ε	Turbulent dissipation rate $(J/Kg \cdot s)$
μ	Dynamic viscosity (kg/ms)
μ_t	Turbulent viscosity (kg/ms)
ρ	Density (kg/m^3)
τ_{ij}	Reynolds stress tensor (kg/s^2m)
Φ	Dissipation function (J/m^3s)
ω	Specific dissipation rate $(J/Kg \cdot s)$

Dimensionless numbers

ε	Relative error (-)
η	Radius ratio (-)
C_D	Drag coefficient (-)
C_P	Pressure coefficient (-)
Ma	Mach number (-)

Re	Reynolds number (-)
y^+	Dimensionless distance from the wall (-)

Acronyms

CFD	Computational Fluid Dynamics
DNS	Direct Numerical Simulation
GCI	Grid Convergence Index
LES	Large Eddy Simulation
$RANS$	Reynolds Averaged Navier Stokes
SST	Shear Stress Transport

Chapter 1

Introduction and Objectives

1.1 Background and Motivation

The classical study and treatment of various scientific and technological problems is conducted through experimental measurements and theoretical models. Most problems of interest in engineering and physical sciences are multidimensional and nonlinear. Consequently, analytical solutions exist only in rare cases. On the other hand, the usage of experimental devices is often quite expensive and time consuming, while in many cases the laboratory conditions differ from the actual ones to a great extent (e.g. scale problems). Therefore, the computational solution of the theoretical problems by using appropriate numerical methods which solve approximately, but with a great accuracy under the appropriate circumstances, the equations that describe the problem, is recommended. There are many cases in engineering applications that cannot be solved analytically, like airplane an automotive aerodynamics, combustion problems, physical and chemical processing problems, weather forecast and climate change problems etc. In all the cases above, the computational solutions leads to a better treatment of these problems as well as to design processes with reduced energy consumption and therefore emissions, as long as we refer to production processes.

Numerical methods analyze in depth the theoretical and mathematical framework which needed to treat the problems mentioned above through techniques and methods of solving the basic categories of partial differential equations which describe the general conservation principles of mass, energy and momentum in a developing in time and space physical or chemical system. The oldest and the simplest numerical method that is applied to solve partial differential equations by transforming them into algebraic equations is the finite differences investigated extensively by Courant, Friedrich and Lewy. The finite elements method was introduced a few years later and was applied in computing forces and strains for materials from structural engineers. The problem with the finite

element method is that it does not treat the nonlinear term properly. The finite volume method is one of the most ingenious methods for discretizing the differential equations which describe a fluid flow field and was scrutinized by Patankar for fluid flows as well as for heat transfer applications [1]. To be more precise, the Navier - Stokes equations along with the continuity equation are discretized and solved numerically in order to describe the physics of the problem and to quantity all of the unknown variables. This analysis, which is more complex that it seems, is called Computational Fluid Dynamics (CFD).

CFD is a powerful tool based on the science of Fluid Mechanics which discretizes the basic differential equations which describe the flow field, the continuity equation and the Navier - Stokes equations, converts them to algebraic equations and a system of equations is created and solved numerically. Additional equations may be introduced when the flow is turbulent, which is the case most engineering applications and physical phenomena. More details about the whole procedure will be given in chapter 3. CFD techniques and in general numerical methods were developed many years ago. However, it was not until a few years ago when they first started to be used in practice because the capability of the computers regarding their frequency and memory were limited. They were used only for academic purposes and in very rare cases for industrial applications, and engineers could not rely on the results. Nevertheless, nowadays due to the rapid increase of available computational resources, quick results from CFD packages can be obtained which is very important for the industry because they need results as soon as possible. Consequently, CFD is considered as a relatively new science which is very promising and it is likely that it will be the predominant in the next decades, replacing the expensive experimental investigation of various applications. Its main advantage is the decreased cost in relation to the experimental process, a very important asset in the current increasingly demanding and competitive environment. Unfortunately, its main drawback is the reliability of the exported results, as when experimental results are not available the results obtained by CFD software are questionable. There are many cases that CFD results are totally unreliable, so scientists and engineers earn no confidence to trust them. As a result, CFD results can only be trusted on specific applications where a comparison with experimental data of similar or even the same applications is successful. Even today, an expensive and carefully designed experiment cannot be replaced by any numerical procedure regarding the reliability of their results, or when it can be replaced, the required time to obtain the results from the numerical procedure is considered as prohibitory for the industry.

1.2 Problem Statement

During the last decades the cost of various types of fossil fuel have increased significantly in most countries, especially in European union where it lacks oil production. Conse-

quently, the cost of transportation has increased dramatically, more than the annual inflation rate of each country. As a result, there have been developed many methods toward decreasing fuel consumption. Another positive impact of reducing fuel consumption is the reduced emissions of CO_2 which is the main responsible gas of global warming, as well as other toxic gases like CO, NO_x, SO_x, particulate matter etc which is of paramount importance regarding the public health as well as the environment. Finally, European union has specified strict limits regarding the emissions mentioned above for power generation and transportation which become stricter year by year and applies penalties when companies do not conform with it. Taking all the above into consideration, it is obvious that energy saving, in general, is of vital importance in any case. Some of the most important and prevalent innovations that have been developed over the last years for reducing the fuel consumption of the vehicles are the optimization of internal combustion engines with higher thermal efficiency and compression ratios, hybrid electric vehicles, other fuel internal combustion engines such as bio diesel or hydrogen, three way catalytic converters with almost zero pressure drop, various types of automatic transmission, vehicles with lower drag coefficients etc.

The present thesis is specialized in the aerodynamic optimization of the front of a bluff body. In particular, 3 different frontal shapes of a bluff body are examined numerically. Bluff bodies can represent very roughly trucks, which are the main means of transportation of basic products like food, furniture, computers, or even smaller in size vehicles. Due to their big size and heavy load, fuel consumption of trucks is high and needs to be reduced as much as possible. Taking into account that the aerodynamic force may account up to 50% of the total fuel consumption on special operating conditions, it is obvious that even small amends on the aerodynamic drag may lead to considerable reductions to fuel consumption, thus a considerable reduction in operating cost of the trucks may be attained.

1.3 Structure of the M.Sc. Thesis

The present thesis starts with a literature survey for bluff bodies in general, but extraordinary consideration was given to the previous studies of DAF Ltd company. Unfortunately, the available literature regarding bluff bodies is rather limited because the topic is somewhat specific. Chapter 3 is exclusively dedicated to the mathematical nature of the problem, describing the governing equations and computational methods that were used, which are almost the same in any CFD application.

As it was stated above, results obtained from CFD commercial packages or even in-house codes are not always reliable. Consequently, validation of CFD results to a similar or even the same geometry with experimental data is of vital importance in order to gain

confidence to investigate numerically theses 3 different frontal shapes of a bluff body. Validation of experimental data was done with Cooper's experiments for bluff bodies in a wind tunnel. The validation process was successful for the fully attached as well as the separated flow around the bluff body. However, it should be kept in mind that these experiments performed by Cooper were held in a wind tunnel while the geometries given by the company was supposed to be held in the free field. In the results and discussion chapter, the optimized geometries are scrutinized from an aerodynamic point of view.

As far as the software are concerned that was used throughout this dissertation, all the simulations were performed with Ansys Fluent v.6, the post processing with Ansys CFX - POST v.14, the grid generation and CAD with Ansys ICEM v.14, the digitization of the graphs with the software Engauge and the graphs with the software Ms Excel. Finally, one of the optimized geometries was created in the software CATIA v.5 since in ICEM elliptical curves cannot be created. The optimization models were given by the company DAF Trucks Ltd.

Chapter 2

Literature Review

Despite the limited literature, there are some scientists who investigated experimentally or numerically the flow around automobiles and proposed ideas for reducing the aerodynamic drag. Cooper has investigated experimentally various types of automobiles starting from bluff bodies to racing cars. He took into account many details like the wind magnitude and direction and he performed his experiments in both stationary and moving ground as well as in open and closed channels for various yaw angles of the vehicle. After various experiments, he found out that for radius ratios over 5% there is no separation and the flow is completely attached for certain Reynolds numbers regardless of the frontal area of the vehicle which is very important because boundary layer separation leads to increased drag. The following image illustrates the bluff body that Cooper used from a 3D point of view. It should be stated that this model was designed by Filip Baillien who investigated this model numerically and validated Cooper's results.

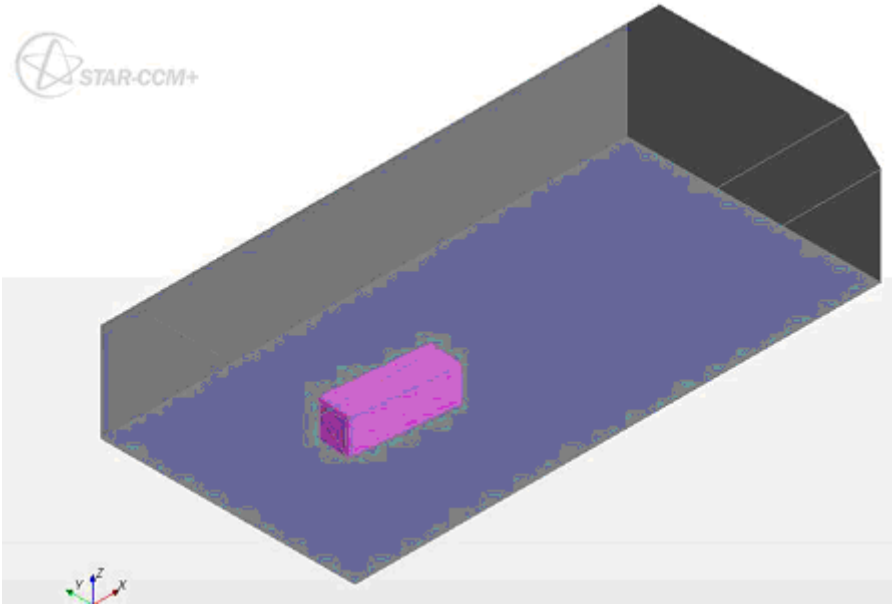

Figure 2.1: Cooper's bluff body and wind tunnel from a 3D point of view.

The following graph shows the drag coefficient of a blunt body for no yaw angle for various front edge radii depending on the Reynolds number.

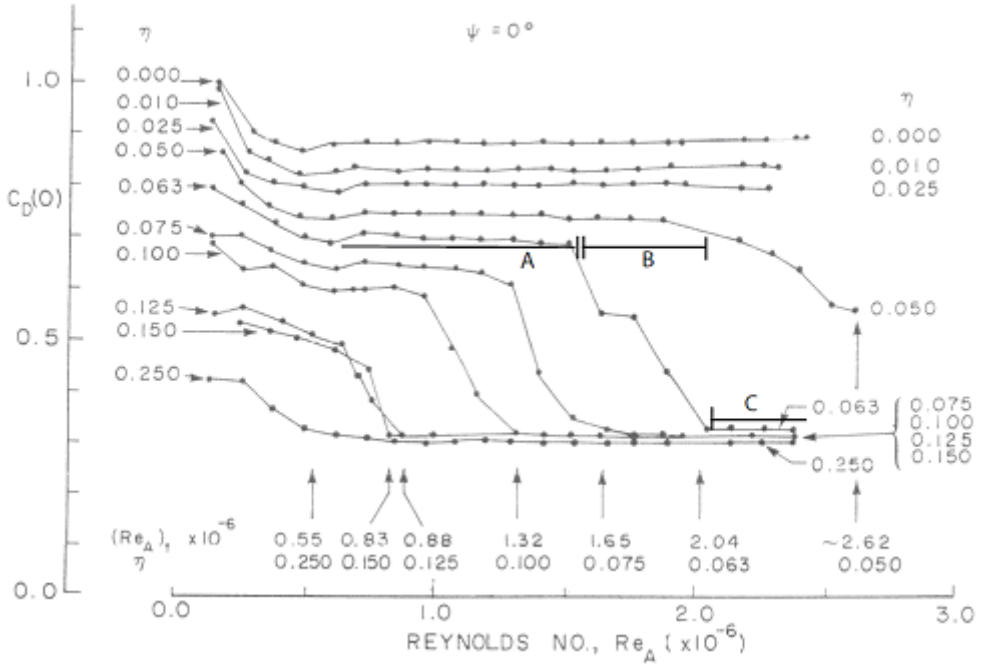

Figure 2.2: Drag coefficient of Cooper's bluff body depending on Reynolds number for various radii for no yaw angle.

Filip Baillien [2] studied numerically the aerodynamic behavior of a simplified truck. He performed RANS steady state simulations and validated Cooper's results for for 7.5% rounding. The following graph shows the results of Cooper's experiment and his numerical results.

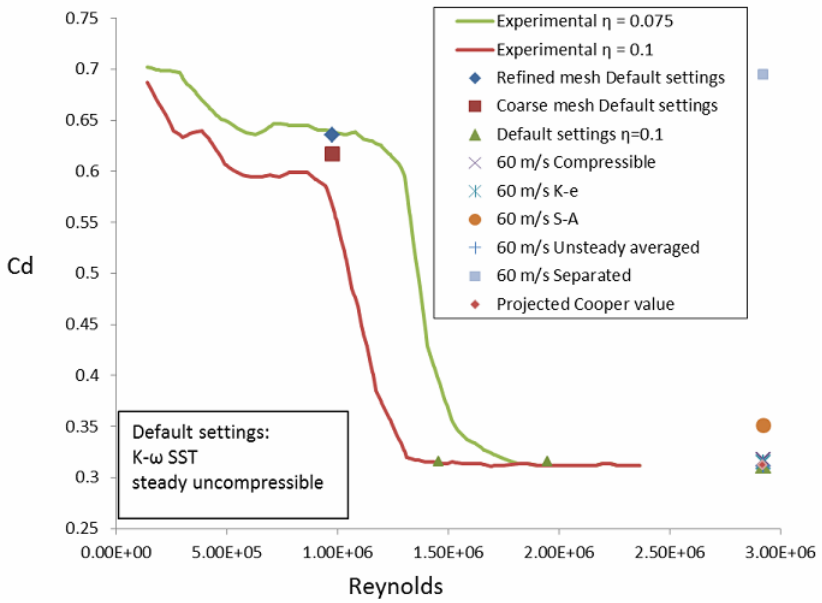

Figure 2.3: Digitized version of Cooper's graph for drag coefficient for radius radii of 7.5% and 10% with some values of Baillien's numerical studies for specific Reynolds numbers.

As seen in the figure above, the differences between transient and steady RANS simulations as well as the results between compressible and incompressible solvers are negligible. As a result, he was relied on the results of steady state simulations and he made a comparison between various turbulent models. A comparative diagram of all turbulent models he used of the pressure coefficient against the vertical centerline of the front of the vehicle.

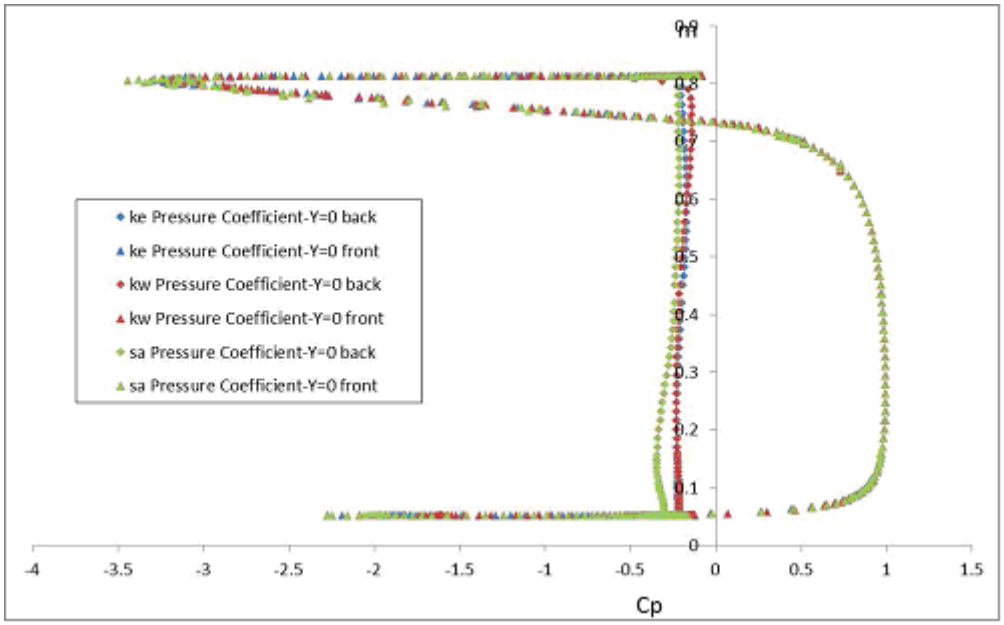

Figure 2.4: Pressure coefficient of the centerline of the front of Cooper's bluff body for various turbulence models.

Also, he managed to reduce, to a small extent, the drag coefficient by making some modifications on the front of the truck. The modifications were based on elliptical curves because other kinds of curves may lead to separation much easier than the elliptical curves. After trying 7 different optimization models he found small differences regarding the drag coefficient. Finally, he proved that the main contribution of the aerodynamic drag is the rear of the truck, not the front because of the separation of the flow and the strong vortices that occur.

J.M.M. Luijten [3] made a more extensive analysis on the truck taking into account many details. More specifically, he found out that the aerodynamic drag accounts for approximately 30% of the total fuel consumption which can arise up to 50% if the truck is empty. This is indicative of the consideration that has to be given on the aerodynamic optimization of the trucks. He also examined a more realistic model of a typical truck without so many simplifications like the previous authors. In detail, he examined 3 different designs of trucks. The first truck model has a gap between the tractor and the trailer, the second is the same model as the first one without the gap and the third model is the Cooper's model. These 3 models are illustrated in the following figures.

Figure 2.5: The 3 models that were investigated numerically by Luijten.

As seen in the first two images above, he also took into account the effects of roof deflectors and side extenders. In addition, he tried 2 types of roof deflectors, one long and one short, for the first 2 models. He was based on steady state simulations, however, he also performed some transient RANS simulations to check any discrepancies on the results. Like Filip Baillien, he found out that the results between steady and unsteady simulations did not differ much. He made many parametric studies on the velocity of the truck for various leading edge radii ratio for various yaw angles. More specifically, he performed simulations for a velocity of 90 $^{km}/_{h}$, 45 $^{km}/_{h}$ and 22.5 $^{km}/_{h}$, however, he was focused mainly on the velocity of 90 $^{km}/_{h}$ because this is the speed of the truck in most of its lifespan. He also performed his simulations for yaw angles varying from 0 to 10º for leading edge radii from 5% to 7.5%. Finally, he made a parametric study on turbulence intensity for 0.5% and 5% at the inlet of the computational domain. The following images represent the drag coefficient for the closed truck model for long and short roof deflectors.

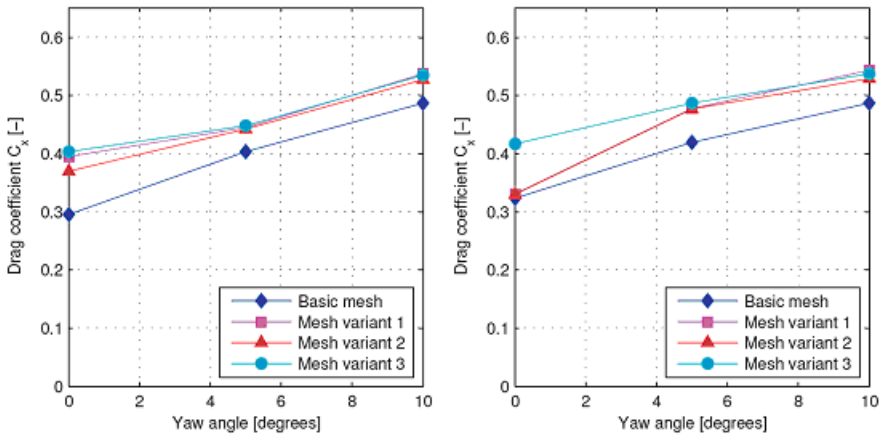

(a) Long roof deflector (b) Short roof deflector

Figure 2.6: Drag coefficient for the long and short roof deflector for the closed truck model for various grids.

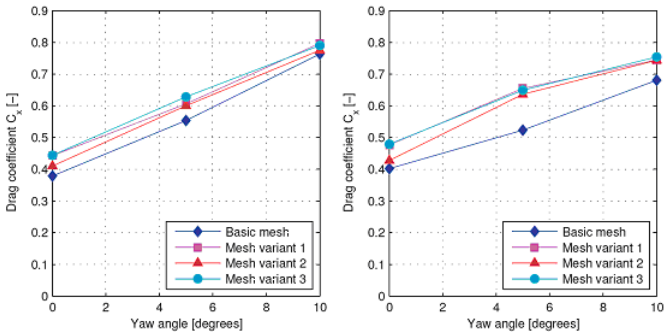

(a) Long roof deflector (b) Short roof deflector

Figure 2.7: Drag coefficient for the long and short roof deflector for the simplified truck model for various grids.

It is clear that the more the yaw angle is the higher the drag coefficient is. This happens because in non zero yaw angles the boundary layer separation is reinforced because the bubble separations are bigger as seen in the figure below.

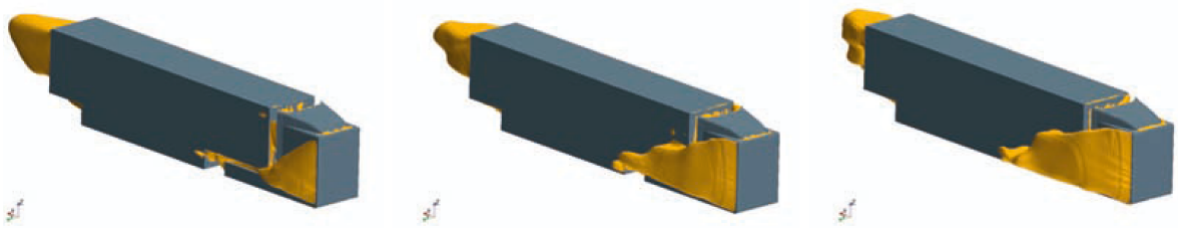

Figure 2.8: Isosurfaces of negative x velocity component for yaw angles of 0°, 5°and10°

The following image illustrates the differences in drag coefficient between the simplified and closed truck models with a long roof deflector for various yaw angles.

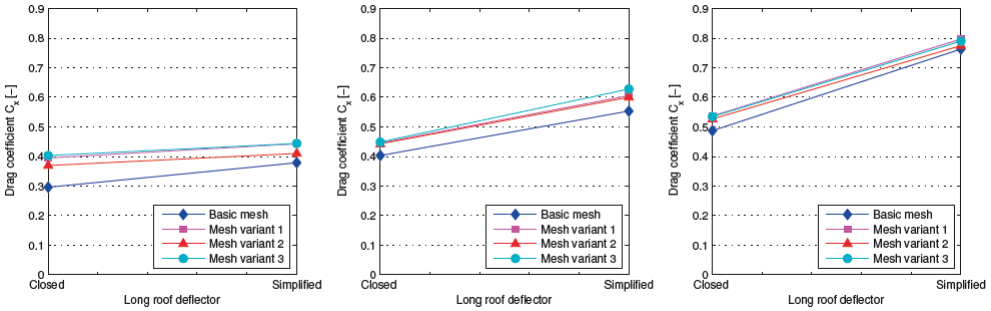

Figure 2.9: Drag coefficients for the closed and simplified truck model for yaw angles of 0°, 5°and10°

As seen in figure 11 above, the closed truck has smaller drag coefficient values for any yaw angle.

The difference in drag coefficient for the long and short roof deflector comes mainly from the separation bubble as seen in figure 12 below. The long roof deflector leads to a decreased separation bubble which reduces the overall drag coefficient.

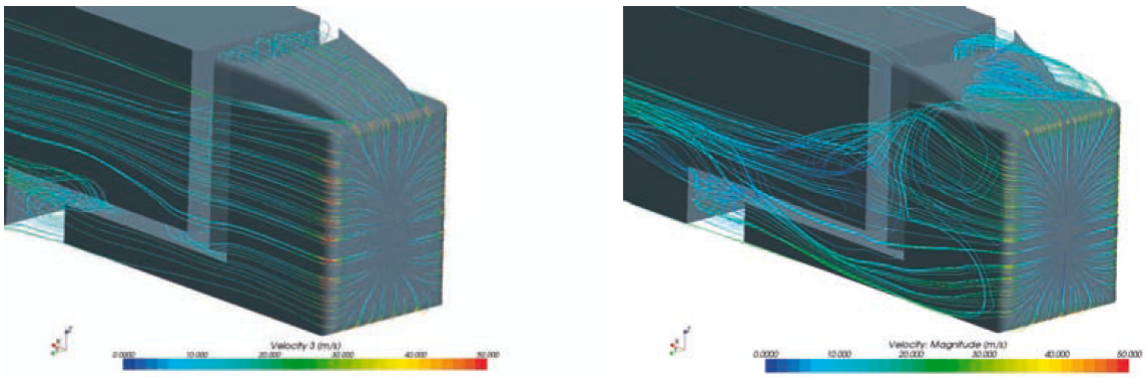

Figure 2.10: Streamline distribution of the front of the simplified truck for a long and a short roof deflector respectively.

The following graph represents the differences in drag coefficient for various yaw angles for the simplified truck model for small and wide side extenders.

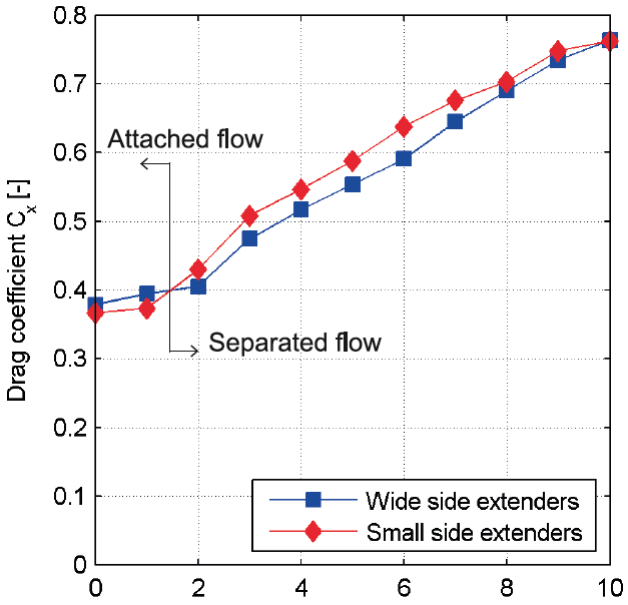

Figure 2.11: Drag coefficient for the simplified truck for various yaw angles with the wide and small side extenders.

As seen in figure 13 above, for very small values of yaw angle the drag coefficient is slightly smaller for wide extenders but it bigger for high yaw angles.

Finally, regarding Cooper's model he found some non negligible variations in drag coefficient with Cooper's model. The following graph represents the comparison in drag coefficient over the leading edge radii of his results and Cooper's results.

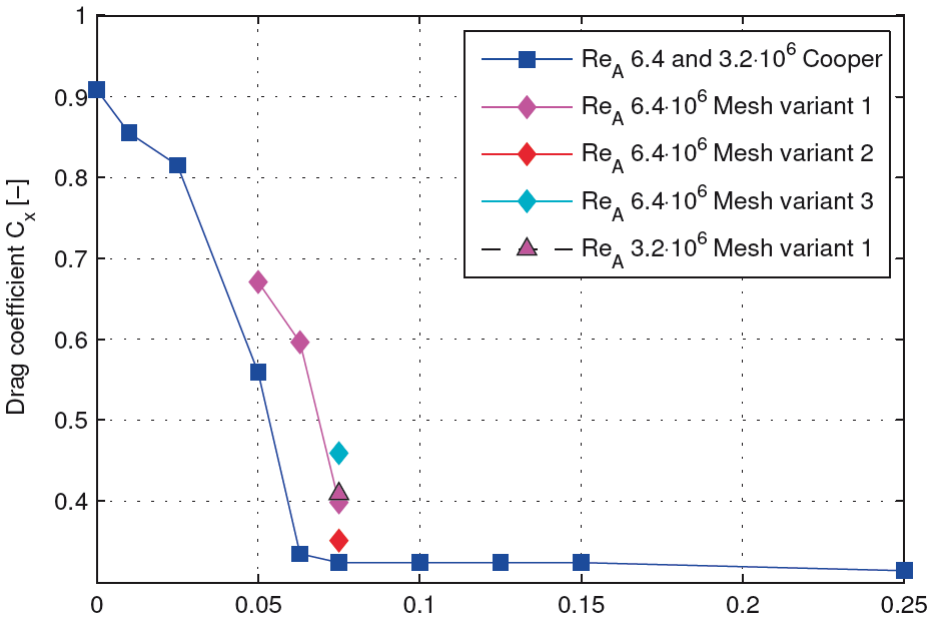

Figure 2.12: Differences in drag coefficient between Cooper's experiments and Luijten's simulations.

One possible explanation for this is that his results were not grid independent and he found some variations between different grid sizes. The following figure shows the bubble separation of the front of Cooper's model according to his results, for various leading edge radius ratio and $Re = 6.4 \cdot 10^6$.

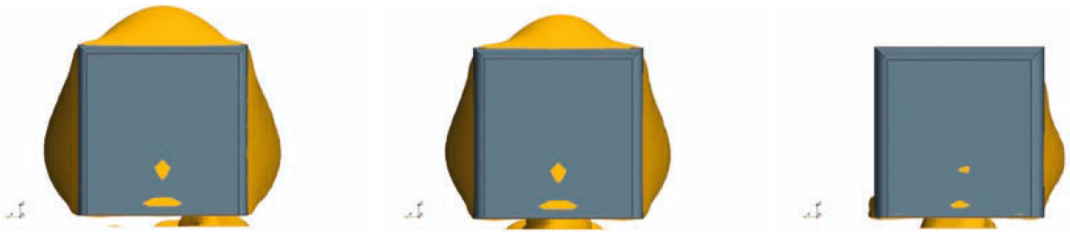

Figure 2.13: Isosurfaces of negative x velocity component for leading radius ratio of 5%, 6.3% and 7.5%.

It is clear from the figure above that even for a leading edge radius ratio of 7.5% boundary layer separation occurs which contradicts Cooper's results.

Bjorn Henneman [4] was focused more on the separation of the boundary layer on the front of a blunt body because, as it was shown above, it plays a dominant role on the calculation of the drag coefficient. Unfortunately, commercial CFD packages do not predict accurately the separation and reattachment point of rounded edges, so unreliable results may be exported by the software regarding the drag coefficient. In order to simplify

the problem, instead of Cooper's model, he used a rounded cylinder (figure 16) because the flow phenomena are the same in both geometries.

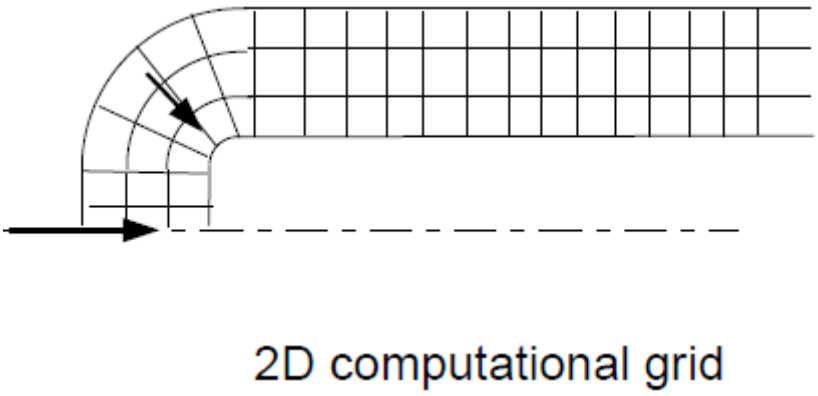

Figure 2.14: Geometry of Henneman's work.

He performed initially some 2D simulations using RANS modeling and showed that for the case of a turbulent flow, the separation point is moving downstream and the reattachment point is moving upstream of the flow as the Reynolds number increases making the separation bubble essentially smaller. Velocity values over the transcritical Reynolds numbers eliminate the separation and the flow becomes fully attached validating essentially Cooper's experiments. He also performed an experiment to double check his results. The following image illustrates the behavior of the separation bubble of a laminar and turbulent boundary layer as the velocity increases.

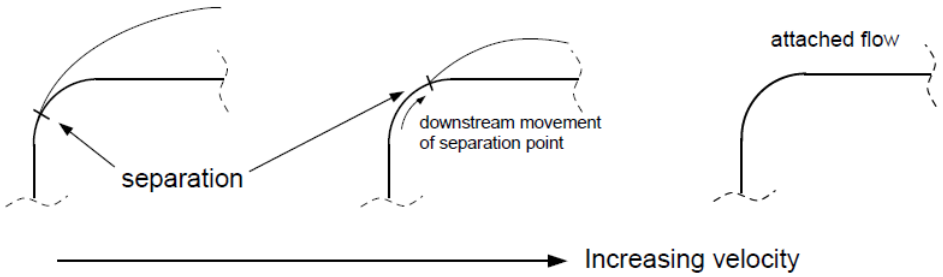

(a) Turbulent

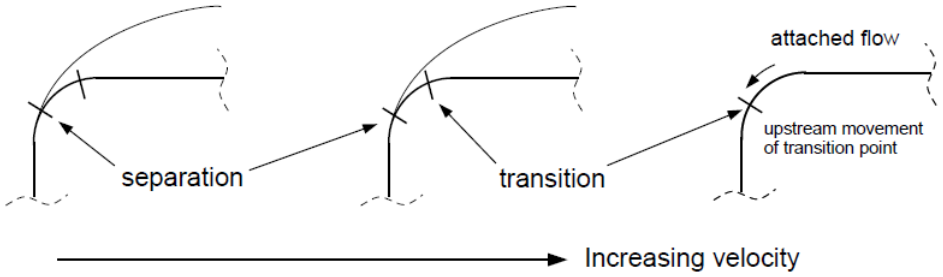

(b) Laminar

Figure 2.15: Separation bubble behavior for a laminar and turbulent boundary layer as the velocity increases.

Unfortunately, all turbulence models he used were proved insufficient in calculating the exact location of the separation point when he compared them with his experiments. More specifically, they tend to underestimate the separation bubble. The following table shows whether or not separation occurs for the Spalart Allmaras model for $Re = 1.2 \cdot 10^6$ for various edge radii and compares them with Cooper's results.

r/D[%]	Separated flow	
	S - A	Cooper
2.5	yes	yes
4	no	yes
5	no	yes
7.5	no	yes
10	no	no

Table 2.1: Separation for $Re = 1.2 \cdot 10^6$ for Spalart Allmaras model and Cooper's experiments.

As seen in the table above, RANS modeling under predicts the separation. Similar or

even worse results were obtained from other turbulence models. This failure of RANS modeling is due to the transitional nature of the flow from laminar to turbulent. However, commercial CFD packages do not include any transitional modeling, so additional modeling is required.

One remedy to this problem lies in the zonal modeling approach. The zonal modeling requires the exact point where the transition occurs which is not known a priori. The position where the separation occurs, can be calculated via an appropriate software such as XFOIL. Once the point where separation occurs, the computational domain is split in laminar and turbulent zone and then they are modeled accordingly by the commercial CFD code. He tried many turbulent models and he concluded that the most favorable is Spalart Allmaras. The following graphs illustrate the difference in drag coefficient for the fully turbulent solution by commercial CFD software and the zonal modeling approach compared with Cooper's results as well as his experimental results for $Re = 1.2 \cdot 10^6$.

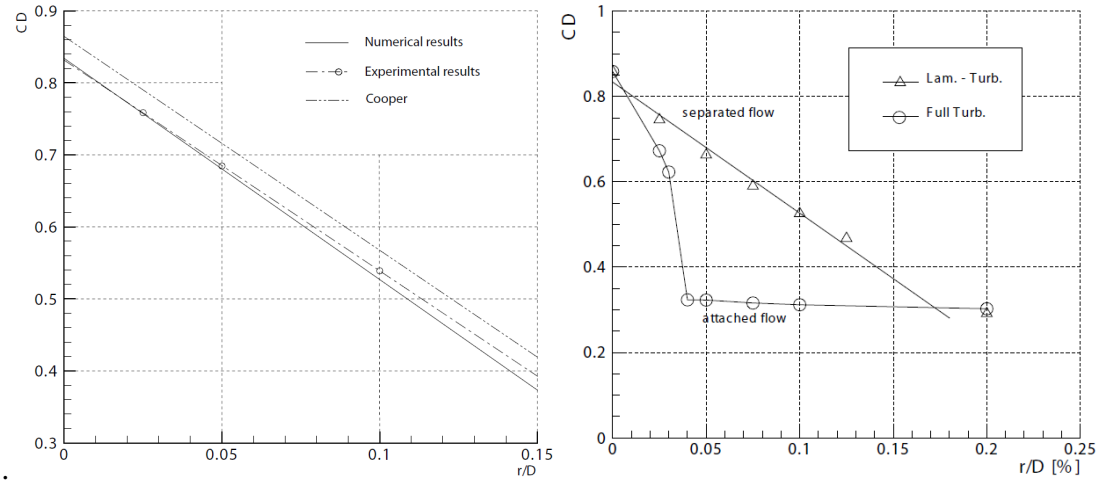

Figure 2.16: Comparative diagrams of drag coefficient among fully turbulent, zonal modeling approach and Cooper's experimental results for a subcritical Reynolds number for various radii ratios.

As seen in figures above, the fully turbulent solution shows an attach behavior for small edge radii ratios which is not true according to Cooper's results. The zonal modeling approach shows the same trend as Cooper's results. However, it should be noted that the zonal approach is appropriate only for the subcritical Reynolds range because a laminar boundary layer separation occurs.

RANS steady state modeling with commercial CFD software was proven adequate for the fully separated or the fully attached region for this application. On the other hand, commercial CFD software does not export reliable results for the transitional region without introducing user defined functions. Due to the fact that the transitional region

appears for law leading edge radii and for low speed magnitude, where the aerodynamic force is relatively small and does not contribute significantly in the fuel consumption of the truck, it is the authors opinion that the thesis should be specialized in the fully attached or fully separated region because, as it will be shown later in this thesis, the flow around the optimized geometries will be fully separated of fully attached, and the rear of the truck which is the main source of the aerodynamic drag, and if possible, to study more complicated models.

Chapter 3

Governing Equations and Computational Methods

3.1 General

The basic equations that describe a flow field are the continuity equation, the 3 Navier - Stokes equations, the energy equation as well as 2 equations of state for a 3D compressible case.

$$\frac{\partial \rho}{\partial t} + div(\rho \vec{u}) = 0 \tag{3.1}$$

$$\frac{\partial (\rho u)}{\partial t} = div(\rho u \vec{u}) = -\frac{\partial P}{\partial x} + div(\mu \cdot gradu) + S_{Mx} \tag{3.2}$$

$$\frac{\partial (\rho v)}{\partial t} = div(\rho v \vec{u}) = -\frac{\partial P}{\partial y} + div(\mu \cdot gradv) + S_{My} \tag{3.3}$$

$$\frac{\partial (\rho w)}{\partial t} = div(\rho w \vec{u}) = -\frac{\partial P}{\partial z} + div(\mu \cdot gradw) + S_{Mz} \tag{3.4}$$

$$\frac{\partial (\rho i)}{\partial t} + div(\rho i \vec{u}) = -Pdiv\vec{u} + div(k \cdot gradT) + \Phi + S_i \tag{3.5}$$

$$P = P_{(\rho,T)} \tag{3.6}$$

$$i = i_{(\rho,T)} \tag{3.7}$$

In this problem the operating fluid is air and considering it as an ideal gas, the last 2 equations are transformed as follows.

$$P = \rho RT \tag{3.8}$$

$$i = C_v T \tag{3.9}$$

The equations above make a total of 7 equations with 7 unknowns, so a system of 7×7 is created and can be solved as long as is it provided with initial and boundary conditions. For reasons that will be explained later in this dissertation, the flow is considered incompressible while heat transfer phenomena do not take place since the flow is incompressible and there are no temperature differences or heat sources anywhere in the domain. Also, there are no chemical reactions and the gravity can be neglected since the density of air is very small. Taking into account all the previous assumptions, the flow field of this specific problem is described by the following equations.

$$div\vec{u} = 0 \tag{3.10}$$

$$\rho\left[\frac{\partial u}{\partial t} + div(u\vec{u})\right] = -\frac{\partial P}{\partial x} + \mu \cdot div(gradu) \tag{3.11}$$

$$\rho\left[\frac{\partial v}{\partial t} + div(v\vec{u})\right] = -\frac{\partial P}{\partial y} + \mu \cdot div(gradv) \tag{3.12}$$

$$\rho\left[\frac{\partial w}{\partial t} + div(w\vec{u})\right] = -\frac{\partial P}{\partial z} + \mu \cdot div(gradw) \tag{3.13}$$

For clarity, by doing some math, the equations above take the following form.

$$\frac{\partial u}{\partial x}+\frac{\partial v}{\partial y}+\frac{\partial w}{\partial z}=0 \tag{3.14}$$

$$\rho\left[\frac{\partial u}{\partial t}+\frac{\partial\left(uu\right)}{\partial x}+\frac{\partial\left(uv\right)}{\partial y}+\frac{\partial\left(uw\right)}{\partial z}\right]=-\frac{\partial P}{\partial x}+\mu\left(\frac{\partial^2 u}{\partial x^2}+\frac{\partial^2 u}{\partial y^2}+\frac{\partial^2 u}{\partial z^2}\right) \tag{3.15}$$

$$\rho\left[\frac{\partial v}{\partial t}+\frac{\partial\left(vu\right)}{\partial x}+\frac{\partial\left(vv\right)}{\partial y}+\frac{\partial\left(vw\right)}{\partial z}\right]=-\frac{\partial P}{\partial y}+\mu\left(\frac{\partial^2 v}{\partial x^2}+\frac{\partial^2 v}{\partial y^2}+\frac{\partial^2 v}{\partial z^2}\right) \tag{3.16}$$

$$\rho\left[\frac{\partial w}{\partial t}+\frac{\partial\left(wu\right)}{\partial x}+\frac{\partial\left(wv\right)}{\partial y}+\frac{\partial\left(ww\right)}{\partial z}\right]=-\frac{\partial P}{\partial z}+\mu\left(\frac{\partial^2 w}{\partial x^2}+\frac{\partial^2 w}{\partial y^2}+\frac{\partial^2 w}{\partial z^2}\right) \tag{3.17}$$

The equations above are the continuity equation and the Navier - Stokes equations which describe fully an unsteady incompressible flow without any chemical reactions or heat transfer phenomena. In the case of a turbulent flow, no analytical functions of the primitive variables exist to solve the Navier - Stokes equations analytically; this can be seen in figure 1 where the fluctuations of the velocity components are abrupt. In Navier - Stokes equations, the term $\frac{\partial u_i u_j}{\partial x_j}$ is called convective term and the term $\frac{\partial^2 u_i}{\partial x_j^2}$ is called diffusive term. In theory, no more information or equations are needed to solve the problem the problem numerically, apart from the initial and boundary conditions. All is needed is the discretization of the equations in order to convert these differential equations to algebraic ones, and an appropriate solver to solve the system of equations that is yielded. However, this procedure would require an extremely refined numerical grid and a very small time step which practically means that it would require years of simulations even at the most powerful clusters, especially for high turbulent flows, which is not practical even for academic purposes, let alone for the industry. This procedure is called Direct Numerical Simulation (DNS), a very accurate method which is used only by researchers for very low Reynolds numbers and it does not seem that it will be used in the near future for industrial purposes. The problem arises with the turbulence because according to this process, it is fully resolved. That is the reason why an extremely refined numerical grid as well as a very small time step are required to yield accurate results from this method.

A remedy to this problem lies in Reynolds Averaged Navier Stokes (RANS) approach firstly introduced by Osborne Reynolds[5]. It is generally known that turbulence is characterized by random and rapid fluctuations of the primitive variables u,v,w and P of the

time and space. Reynolds, instead of the instantaneous values of these variables, he introduced the mean values of them over the time domain. The following figure represents the fluctuations of the u velocity component of a turbulent flow over the time domain.

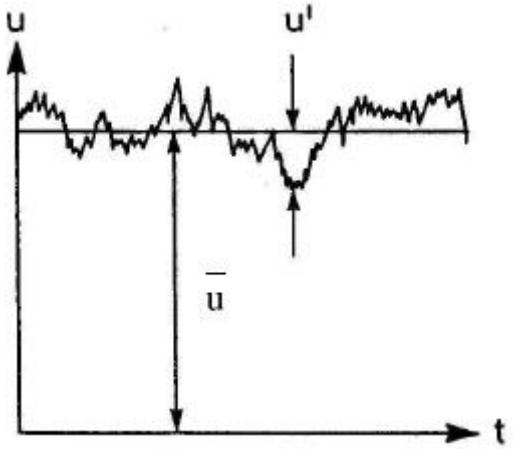

Figure 3.1: Definition of mean and fluctuating turbulent velocity.

The mean value of u velocity component is defined as:

$$\overline{u} = \frac{1}{T}\int_0^T u dt \tag{3.18}$$

where T is a time period which should last more than a period of the fluctuations. The same formula is used for the rest of primitive variables. The fluctuation $u^{'}$ is determined as the deviation of u velocity component from its average value:

$$u^{'} = u - \overline{u} \tag{3.19}$$

Similarly, the rest fluctuating variables are defined:

$$v^{'} = v - \overline{v} \tag{3.20}$$

$$w^{'} = w - \overline{w} \tag{3.21}$$

$$P^{'} = P - \overline{P} \tag{3.22}$$

The mean value of a fluctuating property is equal to zero:

$$\overline{u'} = \frac{1}{T}\int_0^T (u-\overline{u})\,dt = \overline{u}-\overline{u} = 0 \tag{3.23}$$

Substituting the relations 19 - 21 into the continuity equation, the last reduces to:

$$\frac{\partial \overline{u}}{\partial x}+\frac{\partial \overline{v}}{\partial y}+\frac{\partial \overline{w}}{\partial z} \tag{3.24}$$

Substituting these relations also into the Navier - Stokes equations and time averaging them, the Navier - Stokes equations take the following form:

$$\rho\left(\frac{\partial \overline{u}}{\partial t}+\overline{u}\frac{\partial \overline{u}}{\partial x}+\overline{v}\frac{\partial \overline{u}}{\partial y}+\overline{w}\frac{\partial \overline{u}}{\partial z}+\frac{\partial \overline{u'^2}}{\partial x}+\frac{\partial \overline{u'v'}}{\partial y}+\frac{\partial \overline{u'w'}}{\partial z}\right) = -\frac{\partial \overline{P}}{\partial x}+\mu\left(\frac{\partial^2 \overline{u}}{\partial x^2}+\frac{\partial^2 \overline{u}}{\partial y^2}+\frac{\partial^2 \overline{u}}{\partial z^2}\right) \tag{3.25}$$

$$\rho\left(\frac{\partial \overline{v}}{\partial t}+\overline{u}\frac{\partial \overline{v}}{\partial x}+\overline{v}\frac{\partial \overline{v}}{\partial y}+\overline{w}\frac{\partial \overline{v}}{\partial z}+\frac{\partial \overline{u'v'}}{\partial x}+\frac{\partial \overline{v'^2}}{\partial y}+\frac{\partial \overline{v'w'}}{\partial z}\right) = -\frac{\partial \overline{P}}{\partial y}+\mu\left(\frac{\partial^2 \overline{v}}{\partial x^2}+\frac{\partial^2 \overline{v}}{\partial y^2}+\frac{\partial^2 \overline{v}}{\partial z^2}\right) \tag{3.26}$$

$$\rho\left(\frac{\partial \overline{w}}{\partial t}+\overline{u}\frac{\partial \overline{w}}{\partial x}+\overline{v}\frac{\partial \overline{w}}{\partial y}+\overline{w}\frac{\partial \overline{w}}{\partial z}+\frac{\partial \overline{u'w'}}{\partial x}+\frac{\partial \overline{v'w'}}{\partial y}+\frac{\partial \overline{w'^2}}{\partial z}\right) = -\frac{\partial \overline{P}}{\partial z}+\mu\left(\frac{\partial^2 \overline{w}}{\partial x^2}+\frac{\partial^2 \overline{w}}{\partial y^2}+\frac{\partial^2 \overline{w}}{\partial z^2}\right) \tag{3.27}$$

The terms $\overline{u_i'u_j'}$ are called Reynolds stresses or turbulent stresses and they are unknown at this point, so the system of equations is not yet closed. Boussinesq [6] after performing some experiments, correlated the Reynolds stresses to the rate of deformation of the fluid by the following formula for incompressible flows:

$$\tau_{ij} = -\rho\overline{u_i'u_j'} = \mu_t\left(\frac{\partial \overline{u_i}}{\partial x_j}+\frac{\partial \overline{u_j}}{\partial x_i}\right) \tag{3.28}$$

The relation above is called Boussinesq approximation or eddy viscosity assumption and is used by many turbulent models of commercial CFD codes. Substituting Boussinesq relation to the equations 25 - 27, and after doing some math, the latter are transformed as follows:

$$\rho\left(\frac{\partial\overline{u}}{\partial t}+\overline{u}\frac{\partial\overline{u}}{\partial x}+\overline{v}\frac{\partial\overline{u}}{\partial y}+\overline{w}\frac{\partial\overline{u}}{\partial z}\right)=-\frac{\partial\overline{P}}{\partial x}+(\mu+\mu_t)\left(\frac{\partial^2\overline{u}}{\partial x^2}+\frac{\partial^2\overline{u}}{\partial y^2}+\frac{\partial^2\overline{u}}{\partial z^2}\right) \tag{3.29}$$

$$\rho\left(\frac{\partial\overline{v}}{\partial t}+\overline{u}\frac{\partial\overline{v}}{\partial x}+\overline{v}\frac{\partial\overline{v}}{\partial y}+\overline{w}\frac{\partial\overline{v}}{\partial z}\right)=-\frac{\partial\overline{P}}{\partial y}+(\mu+\mu_t)\left(\frac{\partial^2\overline{v}}{\partial x^2}+\frac{\partial^2\overline{v}}{\partial y^2}+\frac{\partial^2\overline{v}}{\partial z^2}\right) \tag{3.30}$$

$$\rho\left(\frac{\partial\overline{w}}{\partial t}+\overline{u}\frac{\partial\overline{w}}{\partial x}+\overline{v}\frac{\partial\overline{w}}{\partial y}+\overline{w}\frac{\partial\overline{w}}{\partial z}\right)=-\frac{\partial\overline{P}}{\partial z}+(\mu+\mu_t)\left(\frac{\partial^2\overline{w}}{\partial x^2}+\frac{\partial^2\overline{w}}{\partial y^2}+\frac{\partial^2\overline{w}}{\partial z^2}\right) \tag{3.31}$$

As it was stated earlier, the turbulence is not resolved but it is modeled according to some turbulence models. Over the years many scientists were involved in turbulence modeling and they created some turbulent models which all of them have pros and cons and there is no right or wrong turbulence model. Each model may perform reasonably for some applications but for some other applications may not be reliable.

3.2 Turbulence models

The most common turbulent model and perhaps the oldest among the 2 equation turbulence models is the standard k - ε model. It is a semi empirical based on the turbulent kinetic energy and dissipation rate. Regarding to its advantages, it is easy to implement, robust and converges relatively easy, and it seems to be reliable for free shear flows. However, it seems to perform poorly for not that high turbulent flows, when strong pressure gradients occur, for rotating flows and it needs a wall function implementation at commercial CFD software. The standard k - ε model consists of the following 2 equations for turbulent kinetic energy and dissipation rate for incompressible flows:

$$\frac{\partial k}{\partial t}+\overline{u_j}\frac{\partial k}{\partial x_j}=\tau_{ij}\frac{\partial\overline{u_i}}{\partial x_j}-\varepsilon+\frac{\partial}{\partial x_j}\left(\frac{\nu+\nu_t}{\sigma_k}\frac{\partial k}{\partial x_j}\right) \tag{3.32}$$

$$\frac{\partial \varepsilon}{\partial t} + \overline{u_j}\frac{\partial \varepsilon}{\partial x_j} = C_{\varepsilon 1}\frac{\varepsilon}{k}\tau_{ij}\frac{\partial \overline{u_i}}{\partial x_j} - C_{\varepsilon 2}\frac{\varepsilon^2}{k} + \frac{\partial}{\partial x_j}\left(\frac{\nu + \nu_t}{\sigma_\varepsilon}\frac{\partial \varepsilon}{\partial x_j}\right) \tag{3.33}$$

In this model, the kinematic eddy viscosity is defined as:

$$\nu_t = C_\mu \frac{k^2}{\varepsilon} \tag{3.34}$$

The system is closed by the following relations and closure coefficients:

$$\omega = \frac{\varepsilon}{C_\mu k} \tag{3.35}$$

$$l = C_\mu \frac{k^{1.5}}{\varepsilon} \tag{3.36}$$

$$C_{\varepsilon 1} = 1.44 \tag{3.37}$$

$$C_{\varepsilon 2} = 1.92 \tag{3.38}$$

$$C_\mu = 0.09 \tag{3.39}$$

$$\sigma_k = 1 \tag{3.40}$$

$$\sigma_\varepsilon = 1.3 \tag{3.41}$$

Taking into account all the drawbacks of the standard k - ε model, some amends were performed in order to improve its performance. One variation of the standard k -

ε model is the RNG k - ε, developed by Yakhot and Orszag. It uses the same equations for turbulent kinetic energy, eddy dissipation rate and kinematic eddy viscosity but it uses different closure coefficients.

$$C_{\varepsilon 2} = \widetilde{C_{\varepsilon 2}} + \frac{C_\mu \lambda^3 \left(1 - \frac{\lambda}{\lambda_0}\right)}{1 + \beta \lambda^3} \tag{3.42}$$

$$\lambda = \frac{k}{\varepsilon} \sqrt{2 S_{ij} S_{ji}} \tag{3.43}$$

$$C_{\varepsilon 1} = 1.42 \tag{3.44}$$

$$\widetilde{C_{\varepsilon 2}} = 1.68 \tag{3.45}$$

$$C_\mu = 0.085 \tag{3.46}$$

$$\sigma_k = 0.72 \tag{3.47}$$

$$\sigma_\varepsilon = 0.72 \tag{3.48}$$

$$\beta = 0.012 \tag{3.49}$$

$$\lambda_0 = 4.38 \tag{3.50}$$

The RNG k - ε model seem to perform better for transitional and separated flows as well as when heat and mass transfer phenomena occur.

Another variation of the standard k - ε model is the realizable k - ε model. It uses the same equation for turbulent kinetic energy but a slightly different equation for the eddy dissipation rate. In particular, the dissipation rate is calculated by the following relation:

$$\frac{\partial \varepsilon}{\partial t} + \overline{u_j}\frac{\partial \varepsilon}{\partial x_j} = C_{\varepsilon 1}\frac{\varepsilon}{k}\tau_{ij}\frac{\partial \overline{u_i}}{\partial x_j} - C_{\varepsilon 2}\frac{\varepsilon^2}{k+\sqrt{\nu\varepsilon}} + \frac{\partial}{\partial x_j}\left(\frac{\nu+\nu_t}{\sigma_\varepsilon}\frac{\partial \varepsilon}{\partial x_j}\right) \tag{3.51}$$

Another difference is that realizable k - ε model uses a function for the variable C_μ instead of constant.

$$C_\mu = \frac{1}{A_0 + A_S\frac{ku^*}{\varepsilon}} \tag{3.52}$$

$$u^* = \sqrt{S_{ij}S_{ij} + \widetilde{\Omega_{ij}}\widetilde{\Omega_{ij}}} \tag{3.53}$$

$$\widetilde{\Omega_{ij}} = \Omega_{ij} - 2\varepsilon_{ijk}\omega_k \tag{3.54}$$

$$\Omega_{ij} = \overline{\Omega_{ij}} - \varepsilon_{ijk}\omega_k \tag{3.55}$$

$$A_0 = 4.04 \tag{3.56}$$

$$A_S = \sqrt{6}cos\phi \tag{3.57}$$

$$\phi = cos^{-1}\left(\sqrt{6}W\right) \tag{3.58}$$

$$W = \frac{S_{ij}S_{jk}S_{ki}}{\tilde{S}^3} \tag{3.59}$$

$$\widetilde{S} = \sqrt{S_{ij}S_{ij}} \tag{3.60}$$

$$S_{ij} = 0.5\left(\frac{\partial \overline{u_j}}{\partial x_i} + \frac{\partial \overline{u_i}}{\partial x_j}\right) \tag{3.61}$$

Finally, the closure coefficients are:

$$C_{\varepsilon 1} = 1.44 \tag{3.62}$$

$$C_{\varepsilon 2} = 1.9 \tag{3.63}$$

$$\sigma_k = 1 \tag{3.64}$$

$$\sigma_\varepsilon 1.2 \tag{3.65}$$

All models described above belong to the family of k - ε turbulence models. Another family of 2 equation turbulence models is the k - ω models. The Wilcox standard k - ω model [6] uses one equation for the turbulent kinetic energy like the family of k - ε models and a transport equation for the specific dissipation rate.

$$\frac{\partial k}{\partial t} + \overline{u_j}\frac{\partial k}{\partial x_j} = \tau_{ij}\frac{\partial \overline{u_i}}{\partial x_j} - \beta^* k\omega + \frac{\partial}{\partial x_j}\left[\left(\nu + \sigma^*\frac{k}{\omega}\right)\frac{\partial k}{\partial x_j}\right] \tag{3.66}$$

$$\frac{\partial \omega}{\partial t} + \overline{u_j}\frac{\partial \omega}{\partial x_j} = \alpha\frac{\omega}{k}\tau_{ij}\frac{\partial \overline{u_i}}{\partial x_j} - \beta\omega^2 + \frac{\sigma_d}{\omega}\frac{\partial k}{\partial x_j}\frac{\partial \omega}{\partial x_j} + \frac{\partial}{\partial x_j}\left[\left(\nu + \sigma\frac{k}{\omega}\right)\frac{\partial \omega}{\partial x_j}\right] \tag{3.67}$$

The system of equations is closed with the following auxiliary relations and closure coefficients:

$$\alpha = \frac{13}{25} \tag{3.68}$$

$$\beta = \beta_0 f_\beta \tag{3.69}$$

$$\beta^* = 0.09 \tag{3.70}$$

$$\sigma = 0.5 \tag{3.71}$$

$$\sigma^* = 0.6 \tag{3.72}$$

$$\sigma_{do} = \frac{1}{8} \tag{3.73}$$

$$\sigma = \begin{cases} 0, & \frac{\partial k}{\partial x_j}\frac{\partial \omega}{\partial x_j} \leq 0 \\ \sigma_{do}, & \frac{\partial k}{\partial x_j}\frac{\partial \omega}{\partial x_j} > 0 \end{cases} \tag{3.74}$$

$$\beta_0 = 0.0708 \tag{3.75}$$

$$f_\beta = \frac{1 + 85\chi_\omega}{1 + 100\chi_\omega} \tag{3.76}$$

$$\chi_\omega = \left| \frac{\Omega_{ij}\Omega_{jk}S_{ki}}{(\beta^*\omega)^3} \right| \tag{3.77}$$

Its main advantage is that it performs well when adverse pressure gradient occurs as well as for transitional flows and it is also stable and robust like the standard k - ε model. A variation of the standard k - ω model is the k - ω Shear Stress Transport (SST) model. Theoretically, it performs better that than the standard k - ε and k - ω models because it combines the advantages of these 2 models. In particular, inside the boundary layer it performs like the k - ω model where it has the advantage of predicting any adverse pressure gradients and in the free field it performs like the standard k - ε model. The SST model comprises the following equations:

$$\frac{\partial k}{\partial t} + \overline{u_j}\frac{\partial k}{\partial x_j} = \frac{\partial}{\partial x_j}\left[\left(\mu + \frac{\mu_t}{\sigma_k}\right)\frac{\partial k}{\partial x_j}\right] - \rho\beta^* k\omega + min\left(G_k, 10\rho\beta^* k\omega\right) \tag{3.78}$$

$$\frac{\partial \omega}{\partial t} + \overline{u_j}\frac{\partial \omega}{\partial x_j} = \left[\left(\mu + \frac{\mu_t}{\sigma_\omega}\right)\frac{\partial \omega}{\partial x_j}\right] + \frac{\alpha}{\nu_t}G_k - \rho\beta\omega^2 + 2\left(1 - F_1\right)\rho\sigma_{\omega 2}\frac{1}{\omega}\frac{\partial k}{\partial x_j}\frac{\partial \omega}{\partial x_j} \tag{3.79}$$

$$\mu_t = \frac{\rho k}{\omega}\frac{1}{max\left[\frac{1}{\alpha^*}, \frac{SF_2}{\alpha_1 \omega}\right]} \tag{3.80}$$

$$\sigma_k = \frac{1}{\frac{F_1}{\sigma_{k1}} + \frac{1-F_1}{\sigma_{k2}}} \tag{3.81}$$

$$\sigma_\omega = \frac{1}{\frac{F_1}{\sigma_{\omega 1}} + \frac{1-F_1}{\sigma_{\omega 2}}} \tag{3.82}$$

$$F_1 = tanh\left(\Phi_1^4\right) \tag{3.83}$$

$$\Phi_1 = min\left[max\left(\frac{\sqrt{k}}{0.09\omega y}, \frac{500\mu}{\rho y^2 \omega}\right), \frac{4\rho k}{\sigma_{\omega 2} D_\omega^+ y^2}\right] \tag{3.84}$$

$$D_\omega^+ = max\left[2\rho\frac{1}{\sigma_{\omega 2}}\frac{1}{\omega}\frac{\partial k}{\partial x_j}\frac{\partial \omega}{\partial x_j}, 10^{-10}\right] \tag{3.85}$$

$$F_2 = tanh\left(\Phi_2^2\right) \tag{3.86}$$

$$\Phi_2 = max\left[2\frac{\sqrt{k}}{0.09\omega y}, \frac{500\mu}{\rho\omega y^2}\right] \tag{3.87}$$

$$G_k = \mu_t\sqrt{2S_{ij}S_{ij}} \tag{3.88}$$

$$\sigma_{k1} = 1.176 \tag{3.89}$$

$$\sigma_{k2} = 1 \tag{3.90}$$

$$\sigma_{\omega 1} = 2 \tag{3.91}$$

$$\sigma_{\omega 2} = 1.168 \tag{3.92}$$

The last turbulence model that was used throughout this dissertation was the one equation model Spalart Allmaras [7]. It was proven the best of all for aerospace applications and gives good results when adverse pressure gradients occur. Another advantage of this model is that it is not that sensitive in grid resolution and y+ which practically means that even a relatively coarse numerical grid for a high y+ value may give better results, in relation to other models. This one equation model does not solve an equation for turbulent kinetic energy, but it solves an equation for the kinematic eddy viscosity. The equations and closure coefficients of Spalart Allmaras model are the following:

$$\frac{\partial\widetilde{\nu}}{\partial t} + \overline{u_j}\frac{\partial\widetilde{\nu}}{\partial x_j} = C_{b1}\widetilde{S}\widetilde{\nu} + \frac{1}{\sigma}\frac{\partial}{\partial x_k}\left[(\nu+\widetilde{\nu})\frac{\partial\widetilde{\nu}}{\partial x_k}\right] + \frac{C_{b2}}{\sigma}\frac{\partial^2\widetilde{\nu}}{\partial x_k^2} - C_{\omega 1}f_\omega\left(\frac{\widetilde{\nu}}{d}\right)^2 \tag{3.93}$$

$$C_{\omega 1} = \frac{C_{b1}}{\kappa^2} + \frac{1 + C_{b2}}{\sigma} \tag{3.94}$$

$$\widetilde{S} = S + \frac{\widetilde{\nu} f_{\upsilon 2}}{\kappa^2 d^2} \tag{3.95}$$

$$S = \sqrt{2\Omega_{ij}\Omega_{ij}} \tag{3.96}$$

$$\Omega_{ij} = 0.5 \left(\frac{\partial \overline{u_i}}{\partial x_j} - \frac{\partial \overline{u_j}}{\partial x_i} \right) \tag{3.97}$$

$$f_{\upsilon 1} = \frac{\chi^3}{\chi^3 + C_{\upsilon 1}^3} \tag{3.98}$$

$$f_{\upsilon 2} = 1 - \frac{\chi}{1 + \chi f_{\upsilon 1}} \tag{3.99}$$

$$\nu_t = \widetilde{\nu} f_{\upsilon 1} \tag{3.100}$$

$$\chi = \frac{\widetilde{\nu}}{\nu} \tag{3.101}$$

$$f_\omega = g \left[\frac{1 + C_{\omega 3}^6}{g^6 + C_{\omega 3}^6} \right]^{\frac{1}{6}} \tag{3.102}$$

$$g = r + C_{\omega 2} \left(r^6 - r \right) \tag{3.103}$$

$$r = \frac{\widetilde{\nu}}{\widetilde{S}\kappa^2 d^2} \tag{3.104}$$

$$\kappa = 0.41 \tag{3.105}$$

$$\sigma = \frac{2}{3} \tag{3.106}$$

$$C_{b1} = 0.1355 \tag{3.107}$$

$$C_{b2} = 0.622 \tag{3.108}$$

$$C_{\upsilon 1} = 7.1 \tag{3.109}$$

$$C_{\omega 2} = 0.3 \tag{3.110}$$

$$C_{\omega 3} = 2 \tag{3.111}$$

3.3 Discretization

All the discussion above was about the equations of fluid flow. These equations need to be discretized in order to enable a numerical solver to solve them. This subsection is involved in the discretization process of the Navier - Stokes equations and the numerical solver of the algebraic system of equations that appears. For simplicity, the analysis that follows is for a case of a 2D laminar flow. The finite volume method is employed to discretize the equations on a staggered grid in order to avoid a possible checkerboard

pressure field. For example, consider a 2D numerical grid like the one illustrated in figure . The discretization of the pressure term in Navier - Stokes equation would yield [8]:

$$\frac{\partial P}{\partial x} = \frac{P_e - P_w}{\Delta x} = \frac{\frac{P_E+P_P}{2} - \frac{P_P+P_W}{2}}{\Delta x} = \frac{P_E - P_W}{2\Delta x} \tag{3.112}$$

As it is seen from the equation above, the central point of the finite volume is missing. This may lead to a checkerboard pressure field which is obviously non realistic. These problems are typical when numerical methods are employed.

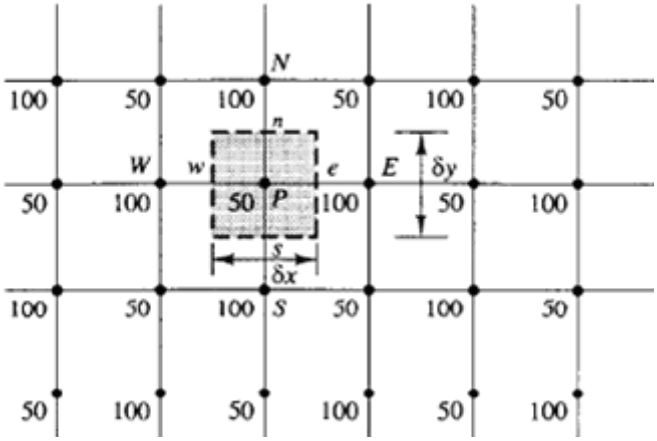

Figure 3.2: Possible pressure profile on a non staggered grid.

A remedy to this problem lies in the idea of the staggered grid. Instead of the original control volume, a half cell toward the west of the original control volume is selected for the discretization of the Navier - Stokes equation in the x direction and a half cell toward the south of the original control volume is selected for the Navier - Stokes equation in the y direction. Figures show these staggered control volumes.

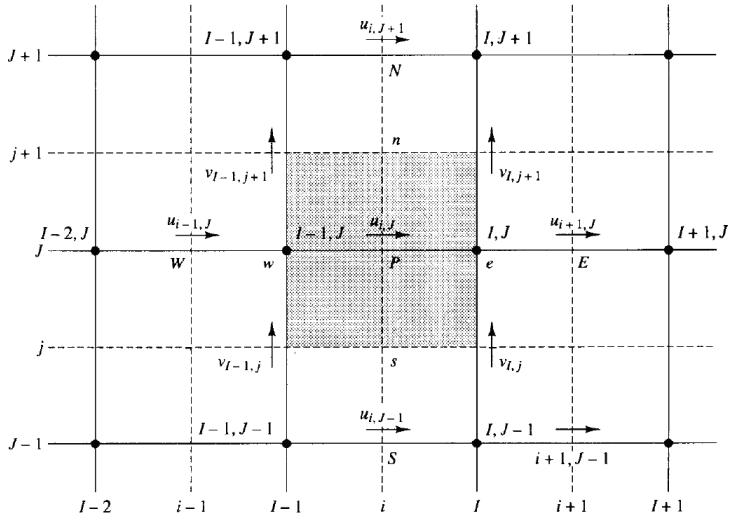

Figure 3.3: The u control volume for the x Navier - Stokes equation.

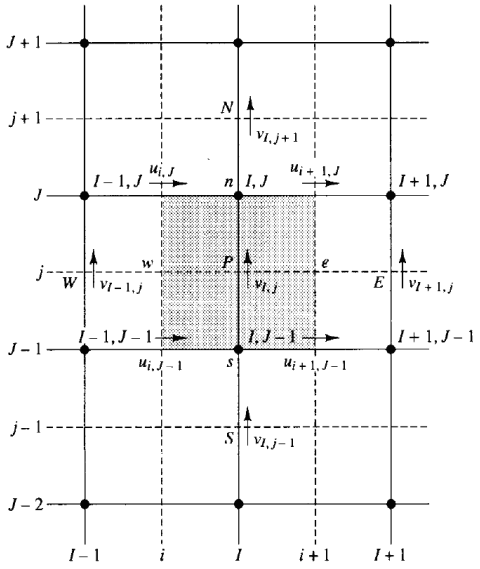

Figure 3.4: The v control volume for the y Navier - Stokes equation.

The diffusive term of the Navier - Stokes equation in the x direction is:

$$\int_V \mu \frac{\partial^2 \overline{u}}{\partial x^2} dV + \int_V \mu \frac{\partial^2 \overline{u}}{\partial y^2} dV = \mu \int_A n \cdot \frac{\partial^2 \overline{u}}{\partial x^2} dA + \mu \int_A n \cdot \frac{\partial^2 \overline{u}}{\partial y^2} dA =$$

$$\mu\left[\frac{\partial\overline{u}}{\partial x}A\right]_e-\mu\left[\frac{\partial\overline{u}}{\partial x}A\right]_w+\mu\left[\frac{\partial\overline{u}}{\partial y}A\right]_n-\mu\left[\frac{\partial\overline{u}}{\partial y}A\right]_s=$$

$$\mu\left[\frac{\overline{u_E}-\overline{u_P}}{\Delta x_e}\right]A_e-\mu\left[\frac{\overline{u_P}-\overline{u_W}}{\Delta x_w}\right]A_w+\mu\left[\frac{\overline{u_N}-\overline{u_P}}{\Delta y_n}\right]A_n-\mu\left[\frac{\overline{u_P}-\overline{u_S}}{\Delta x_s}\right]A_s \tag{3.113}$$

Since the grid is 2D, the areas that appear in each term are not areas but essentially lengths. Considering for simplicity that the grid is uniform in each direction, which practically means that the quantities Δx and Δy are stable throughout the domain, the term above is simplified as follows:

$$\mu\left[\frac{\overline{u_E}-\overline{u_P}}{\Delta x}\right]\Delta y-\mu\left[\frac{\overline{u_P}-\overline{u_W}}{\Delta x}\right]\Delta y+\mu\left[\frac{\overline{u_N}-\overline{u_P}}{\Delta y}\right]\Delta x-\mu\left[\frac{\overline{u_P}-\overline{u_S}}{\Delta y}\right]\Delta x=$$

$$D_e\left(\overline{u_E}-\overline{u_P}\right)-D_w\left(\overline{u_P}-\overline{u_W}\right)+D_n\left(\overline{u_N}-\overline{u_P}\right)-D_s\left(\overline{u_P}-\overline{u_S}\right) \tag{3.114}$$

where

$$D_e=D_w=\frac{\mu\Delta y}{\Delta x} \tag{3.115}$$

$$D_n=D_s=\frac{\mu\Delta x}{\Delta y} \tag{3.116}$$

The integration of the convective term is proceeded as follows:

$$\rho\int_V\frac{\partial\left(\bar{u}\bar{u}\right)}{\partial x}dV+\rho\int_V\frac{\partial\left(\bar{u}\bar{v}\right)}{\partial x}dV=\rho\int_A n\cdot\bar{u}\bar{u}dA+\rho\int_A n\cdot\bar{u}\bar{v}dA=$$

$$\rho\left(\bar{u}\bar{u}A\right)_e-\rho\left(\bar{u}\bar{u}A\right)_w+\rho\left(\bar{u}\bar{v}A\right)_n-\rho\left(\bar{u}\bar{v}A\right)_s=$$

$$\frac{\overline{u_{i+1,J}}+\overline{u_{i,J}}}{2}\rho\Delta y\overline{u_e}-\frac{\overline{u_{i-1,J}}+\overline{u_{i,J}}}{2}\rho\Delta y\overline{u_w}+\frac{\overline{u_{i,J+1}}+\overline{u_{i,J}}}{2}\rho\Delta x\overline{u_n}-\frac{\overline{u_{i,J-1}}+\overline{u_{i,J}}}{2}\rho\Delta x\overline{u_s}=$$

$$F_e\overline{u_e}-F_w\overline{u_w}+F_n\overline{u_n}-F_s\overline{u_s} \tag{3.117}$$

where

$$F_e=\frac{\overline{u_{i+1,J}}+\overline{u_{i,j}}}{2}\rho\Delta y \tag{3.118}$$

$$F_w=\frac{\overline{u_{i-1,J}}+\overline{u_{i,j}}}{2}\rho\Delta y \tag{3.119}$$

$$F_n=\frac{\overline{u_{i,J+1}}+\overline{u_{i,j}}}{2}\rho\Delta x \tag{3.120}$$

$$F_e=\frac{\overline{u_{i,J-1}}+\overline{u_{i,j}}}{2}\rho\Delta x \tag{3.121}$$

Finally, the integration of the pressure gradients yields:

$$-\int_V\frac{\partial P}{\partial x}=-\frac{\overline{P_{I,J}}-\overline{P_{I-1,J}}}{\Delta x}\Delta V=\left(\overline{P_{I-1,J}}-\overline{P_{I,J}}\right)\Delta y \tag{3.122}$$

Assembling all of these terms together, and assuming that the flow is steady state, which practically means that the time derivative is equal to zero, the final form of the discretized Navier - Stokes equation in the x direction, following the notation of the figures becomes:

$$F_e\overline{u_e}-F_w\overline{u_w}+F_n\overline{u_n}-F_s\overline{u_s}=\left(\overline{P_{I-1,J}}-\overline{P_{I,J}}\right)\Delta y+$$

$$+D_e\left(\overline{u_{i+1,J}}-\overline{u_{i,J}}\right)-D_w\left(\overline{u_{i,J}}-\overline{u_{i-1.J}}\right)+D_n\left(\overline{u_{i,J+1}}-\overline{u_{i,J}}\right)-D_s\left(\overline{u_{i,J}}-\overline{u_{i,J-1}}\right) \quad (3.123)$$

The assumption of steady state will be discussed in the next chapter. In a similar way, the discretized Navier - Stokes equation in the y direction is:

$$F_e\overline{v_e}-F_w\overline{v_w}+F_n\overline{v_n}-F_s\overline{v_s}=\left(\overline{P_{I,J}}-\overline{P_{I,J-1}}\right)\Delta x+$$

$$D_e\left(\overline{v_{I+1,j}}-\overline{v_{I,j}}\right)-D_w\left(\overline{v_{I,j}}-\overline{v_{I-1,j}}\right)+D_n\left(\overline{v_{I,j+1}}-\overline{v_{I,j}}\right)-D_s\left(\overline{v_{I,j}}-\overline{v_{I,j-1}}\right) \quad (3.124)$$

where

$$F_e=\frac{\overline{u_{i+1,J}}+\overline{u_{i+1,J-1}}}{2} \quad (3.125)$$

$$F_w=\frac{\overline{u_{i,J}}+\overline{u_{i,J-1}}}{2} \quad (3.126)$$

$$F_n=\frac{\overline{v_{I,j+1}}+\overline{v_{I,j}}}{2} \quad (3.127)$$

$$F_s=\frac{\overline{v_{I,j}}+\overline{v_{I,j-1}}}{2} \quad (3.128)$$

The coefficients of D are the same as in Navier - Stokes equation in x direction. It should be stated here that the velocity components which are inside the F and D coefficients are calculated from the previous step, so they are known values. The Navier - Stokes equations can be written in a more compact form for simplicity:

$$\alpha_{i,J}u_{i,J}=\sum\alpha_{nb}u_{nb}-\left(P_{I,J}-P_{I-1,J}\right)\Delta y \quad (3.129)$$

$$\alpha_{I,j} v_{I,j} = \sum \alpha_{nb} v_{nb} - (P_{I,J} - P_{I,J-1})\,\Delta x \tag{3.130}$$

Discretization scheme

As it was seen in the previous subsector, the velocity values are not stored on the cell faces, Consequently, the left part of the Navier - Stokes equations needs further treatment in order to enable the user to solve them. The velocities on the cell faces are treated according to the discretization scheme that is used. For better accuracy, the third order MUSCL scheme was used throughout this project for the momentum equation. The third order MUSCL scheme is given by the following formula [7]:

$$\phi_f = \theta \cdot \phi_{f,CD} + (1-\theta)\,\phi_{f,SOU} \tag{3.131}$$

where

$$\phi_{f,SOU} = \phi + \nabla\phi \bullet \overrightarrow{r} \tag{3.132}$$

and

$$\phi_{f,CD} = 0.5\,(\phi_0 + \phi_1) + 0.5\,(\nabla\phi_0 \bullet \overrightarrow{r_0} + \nabla\phi_1 \bullet \overrightarrow{r_1}) \tag{3.133}$$

The variable ϕ is essentially the averaged velocity $\overline{u}$. For clarity, the quantity $\phi_{f,SOU}$ is analyzed below:

$$\phi_{f,SOU} = \phi + \left(\frac{\partial\phi}{\partial x}\overrightarrow{i} + \frac{\partial\phi}{\partial y}\overrightarrow{j}\right) \bullet \left(x\overrightarrow{i} + y\overrightarrow{j}\right) = \phi + x\frac{\partial\phi}{\partial x} + y\frac{\partial\phi}{\partial y} \tag{3.134}$$

The computed variables are substituted in the equations 123 and 124.

The simplest and the oldest way for solving the discretized Navier - Stokes equations is the Simple algorithm. The concept of this algorithm is explained below [8]. At first, a pressure field is guessed. For simplicity, the dashes over the unknown variables are omitted.

$$P^* = P - P' \tag{3.135}$$

Now, the guessed pressure field is introduced into the two momentum equations and the latter equations are solved to obtain the corresponded guessed velocity components (u^*, v^*).

$$u^* = u - u' \tag{3.136}$$

$$v^* = v - v' \tag{3.137}$$

where P',u',v' are the deviations of the variables' actual values.
The momentum equations with the guessed values are:

$$\alpha_{i,J} u^*_{i,J} = \sum \alpha_{nb} u^*_{nb} - \left(P^*_{I,J} - P^*_{I-1,J}\right) \Delta y \tag{3.138}$$

$$\alpha_{I,j} v^*_{I,j} = \sum \alpha_{nb} v^*_{nb} - \left(P^*_{I,J} - P^*_{I,J-1}\right) \Delta x \tag{3.139}$$

The above equations are subtracted from the original Navier - Stokes equations (129) and (130) which yields:

$$\alpha_{i,J} \left(u_{i,J} - u^*_{i,J}\right) = \sum \alpha_{nb} \left(u_{nb} - u^*_{nb}\right) + \left[\left(P_{I-1,J} - P^*_{I-1,J}\right) - \left(P_{I,J} - P^*_{I,J}\right)\right] \Delta y \tag{3.140}$$

...

$$\alpha_{I,j} \left(v_{I,j} - v^*_{I,j}\right) = \sum \alpha_{nb} \left(v_{nb} - v^*_{nb}\right) + \left[\left(P_{I,J-1} - P^*_{I,J-1}\right) - \left(P_{I,J} - P^*_{I,J}\right)\right] \Delta x \tag{3.141}$$

Using the correction formulas (135), (136) and (137) the above equations are transformed to:

$$\alpha_{i,J} u'_{i,J} = \sum \alpha_{nb} u'_{nb} - \left(P^{*\prime}_{I,J} - P'_{I-1,J}\right) \Delta y \tag{3.142}$$

$$\alpha_{I,j} v'_{I,j} = \sum \alpha_{nb} v'_{nb} - \left(P'_{I,J} - P'_{I,J-1}\right) \Delta x \tag{3.143}$$

At this point, the terms $\sum \alpha_{nb} u'_{nb}$ and $\sum \alpha_{nb} v'_{nb}$ are omitted from the equations (142) and (143). This is the main approximation of the Simple algorithm. In the end, this approximation will not affect the results because, as the solution converges, the magnitude of values u' and v' will be very small, so these terms will be close to zero. Consequently, the momentum equations are simplified as follows:

$$u'_{i,J} = d_{i,J}\left(P'_{I-1,J} - P'_{I,J}\right) \tag{3.144}$$

$$v'_{I,j} = d_{I,j}\left(P'_{I,J-1} - P'_{I,J}\right) \tag{3.145}$$

where

$$d_{i,J} = \frac{\Delta y}{\alpha_{i,J}} \tag{3.146}$$

$$d_{I,j} = \frac{\Delta x}{\alpha_{I,j}} \tag{3.147}$$

The correction formulas for the two velocity components (136) and (137) are again substituted in the formulas (144) and (145):

$$u_{i,J} = u^*_{i,J} + d_{i,J}\left(P'_{I-1,J} - P'_{I,J}\right) \tag{3.148}$$

$$v_{I,j} = v^*_{I,j} + d_{I,j}\left(P'_{I,J-1} - P'_{I,J}\right) \tag{3.149}$$

The two equations above can be considered also for the points i+1, J and I,j+1:

$$u_{i+1,J} = u^*_{i+1,J} + d_{i+1,J}\left(P'_{I,J} - P'_{I+1,J}\right) \tag{3.150}$$

$$v_{I,j+1} = v^*_{I,j+1} + d_{I,j+1}\left(P'_{I,J} - P'_{I,J+1}\right) \tag{3.151}$$

The continuity equation is discretized throughout the original control volume (Figure 3.2) which yields:

$$(u\Delta y)_{i+1,J} - (u\Delta y)_{i,J} + (v\Delta x)_{I,j+1} - (v\Delta x)_{I,j} = 0 \tag{3.152}$$

If the equations (148) – (151) are substitute in the equation (152) the only unknown values are the $P^{'}$ values. So, the system of equations is solved to compute the $P^{'}$ values. Once the $P^{'}$ values are known, the P values are calculated via the relation (135) and the velocity components u, v are calculated via the the relations (136) and (137). The values u, v, P obtained from this procedure will now be the new guessed values. The same procedure is continued until or if the convergence criteria are satisfied. In the present thesis, the specified convergence criteria are 10^{-5}. This practically means that the values from one iteration to the next should not differ more than 10^{-5}. The Simple algorithm does not always reach a converged solution. It is susceptible to divergence which depends mainly on the quality of the grid and the discretization scheme. Given these two parameters, a method that helps the Simple algorithm to converge is the under - relaxation method. The under - relaxation method lies on some coefficients on the correction formulas. These coefficients take values between 0 and 1. In particular, instead of the formula (35) it can be used the formula:

$$P = P^{*} + \alpha_P P^{'} \tag{3.153}$$

The under - relaxation methods can also be applied to velocities:

$$u = \alpha_u u^{'} + (1 - a_u)\, u^{*} \tag{3.154}$$

$$v = \alpha_u v^{'} + (1 - \alpha_u)\, v^{*} \tag{3.155}$$

If the under - relaxation factors are close to 1 and the initial guessed values are very far from the actual ones, the algorithm is susceptible to divergence. If the under – relaxation factors are close to 0 the algorithm will be very slow to converge because it will apply almost no correction. In the present thesis, all under - relaxation coefficients were left to their default values.

The last step of the Simple algorithm is the solution of the system of equations that was produced during this procedure. The system of equations is a tridiagonal matrix and

its general form is presented below:

$$\begin{bmatrix} b_1 & c_1 & 0 & 0 & 0 \\ a_2 & b_2 & c_2 & 0 & 0 \\ 0 & a_3 & b_3 & ... & 0 \\ 0 & 0 & ... & ... & c_n \\ 0 & 0 & 0 & a_n & b_n \end{bmatrix} \cdot \begin{bmatrix} x_1 \\ x_2 \\ x_3 \\ ... \\ x_n \end{bmatrix} = \begin{bmatrix} y_1 \\ y_2 \\ y_3 \\ ... \\ y_n \end{bmatrix} \tag{3.156}$$

where x are the unknown values, a, b, c are the coefficients of the unknowns and y are known values as well. Based on the Gaussian elimination method, the unknown values of x can be computed.

Summarizing the whole concept and techniques of CFD it can be observed that the whole procedure contains a lot of errors. The errors are assembled and presented below [9]:

- Discretization error

The computational domain cannot be discretized into infinite points. A sensible number of elements should be chosen after performing a Grid Convergence Study. The concept of Grid Convergence Study will be discussed and applied in the next chapter. To make matters worse, experience with CFD showed that sometimes, extremely refined numerical grids can lead to worse results in relation to medium sized grids. By discretizing the domain, however, some information is lost which introduces an error to the final solution.

- Turbulence modeling

The overwhelming majority of flows in nature and engineering are turbulent. As it was stated earlier, the turbulence is not resolved in RANS simulations as it would require a very refined grid which is not practical. The turbulence is modeled by the approximations showed earlier in this chapter which introduce an error. Depending on the application, this error can be the largest error among all steps of the CFD concept.

- Truncation error

Computers cannot store infinite digits for the variables. Modern computers can store up to 64 digits and the rest are truncated. This error can be significant when the simulation requires a large number of iterations until convergence.

- Convergence criteria

Theoretically, the values of each variable should not differ at all from the previous iteration. However, it is not possible to specify the convergence criteria to the limits of

the computer's storage capacity. Even if it was possible it would not be practical, as the simulation would require millions or even billions of iterations. Also, in that case the truncation error explained above would be high and the results would be by far from reality.

- Compressibility effect

This is not the case for every CFD simulation because compressible solvers can be applied to commercial CFD software or in - house codes. However, in the present thesis, an incompressible solver was applied for all simulations. The reasons for this selection will be discussed in the next chapter. Also, experience with CFD showed that sometimes compressible solvers do not perform properly for low velocity flows. However, applying an incompressible solver for simulating a compressible fluid, e.g. air in this case, introduces an extra error.

- Continuum hypothesis

The fluids in CFD simulations are considered to be continuous. From a macroscopic point of view it seems to be true. However, from a microscopic point of view the all the fluids consist of molecules, so the continuum hypothesis is not 100% accurate which contributes also to a minor error in the final results.

- Viscous term

The viscous term in the momentum equations is treated by the assumption made by Navier and Stokes. This assumption was based on their observations and experiments. This assumption seems to be close to reality since it has not been changed over the last 100 years, however, it adds a very small error in the results.

The last two errors seem to be the least significant errors and are beyond the scope of the science of CFD and the present thesis. Rather, it is a topic for research in Physics, Engineering or even Mathematics because the latter is the only available language to express the physical phenomena. The most significant error in the vast majority of CFD simulations is the turbulence modeling as it is kind of unknown what exactly it is resolved regarding the turbulence and the turbulence models are used as "black boxes". This is the reason, as it was stated earlier, why LES (Large Eddy Simulation) simulations are more reliable and closer to the actual values because most of the length scales are resolved. The LES approach is roughly, the intermediate step between the RANS and the DNS concepts. It is known that the turbulence consists of various sizes of length scales which glow and decay at random by exchanging energy from the larger scales to the smaller. The LES approach lies in resolving the large scales and modeling the small ones. Further analysis of this approach, however, is beyond the scope of the present thesis and is not further

analyzed. Unfortunately, the limited available time and computer resources were a big obstacle to perform so many simulations with LES modeling, so all the presented results in the next chapters are based on RANS modeling. Finally, regarding the frequency of the processors, for a numerical grid consisting of $6.25 \cdot 10^6$ elements, using 8 processors per simulation, 6000 iterations which was an adequate number of iterations for achieving convergence in most of the cases, required approximately 8 hours.

Chapter 4

Validation and verification

4.1 General

As it was stated at a previous chapter, results from commercial CFD packages or even in - house codes cannot be trusted without any clue of confidence. Experimental data for the geometries that were simulated during this dissertation are not available. Consequently, the validation process took place on Cooper's bluff bodies that were shown earlier in literature review chapter. By taking a closer look on these optimized geometries, it is obvious that for high Reynolds numbers for the first 2 models, the rectangular box and the simplified truck model, the flow is separated due to their sharp edges. while for the third model, the model with the rounded frontal area, the flow is fully attached. These assumption will be proven later throughout the present dissertation. Taking into consideration these assumptions, the validation of Cooper's experiments should be performed for both of these cases. The dimensions of bluff body that Cooper used for his experiments, as well as the tunnel that he used are presented below [10].

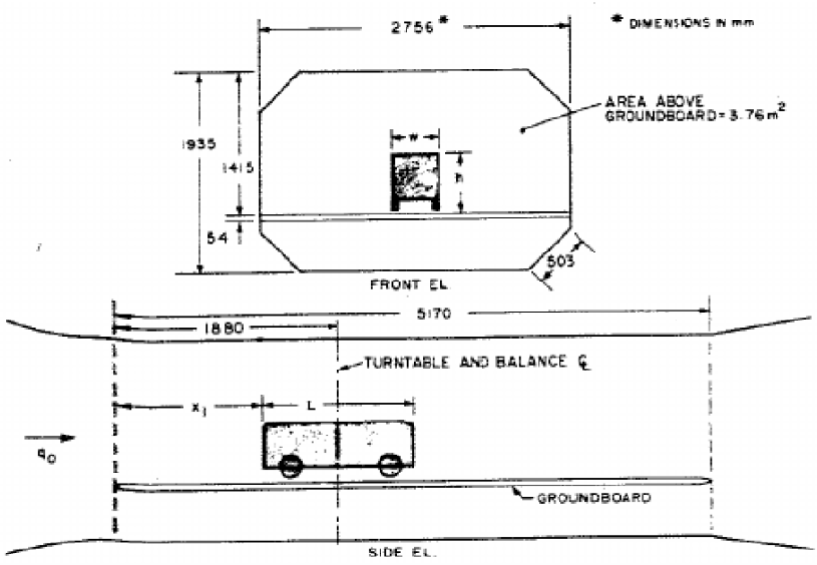

Figure 4.1: Dimensions of Cooper's body and wind tunnel.

The dimensions of Cooper's bluff body are presented in the following table.

Length (m)	1.143
Width (m)	0.381
Height (m)	0.3808
Ground clearance (m)	0.0256

Table 4.1: Dimensions of Cooper's bluff body.

The characteristic length for the definition of Reynolds number was the square root of the frontal area of the bluff body. So, for all of his parametric studies the characteristic length that he used was:

$$D = \sqrt{A} = \sqrt{0.3808 \times 0.381} = 0.3809m \tag{4.1}$$

As leading edge radius ratio he defined the radius of the edges of the frontal area divided with the characteristic length of the bluff body:

$$\eta = \frac{r}{D} = \frac{r}{0.3809} \tag{4.2}$$

The following graph illustrates the drag coefficient of his bluff body, for various Reynolds numbers, for various radius ratio, for angles of attack of 0°and 10°.[11]

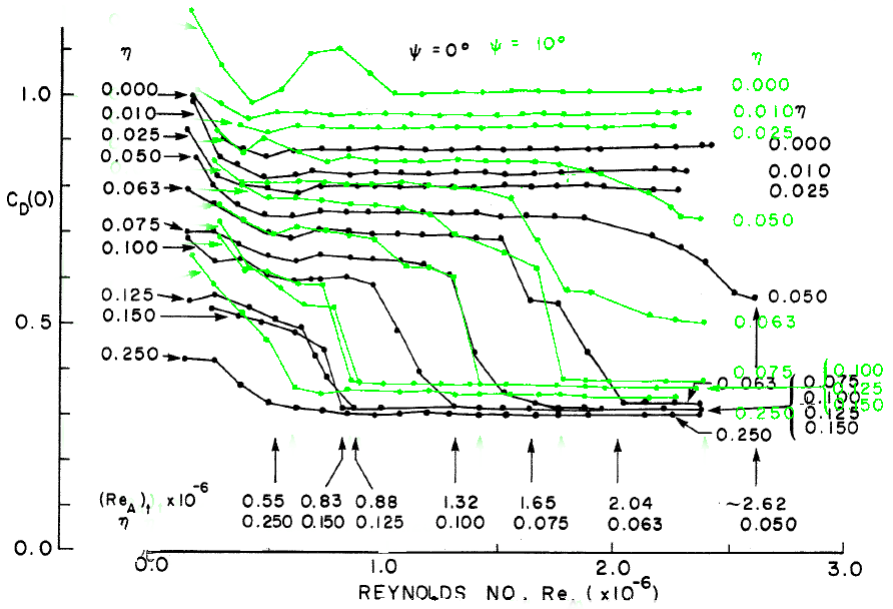

Figure 4.2: Drag coefficient of Cooper's bluff body for various Reynolds numbers for various leading edge radius ratio for 0°and 10°yaw angle.

This graph can be separated into 3 regions. The fully separated region where the drag coefficient is high and it appears for low Reynolds numbers, for low radius ratio of the frontal area. The fully attached region where the drag coefficient has its lowest potential value, given the geometrical features and it occurs at high Reynolds numbers for high radius ratios of the frontal area. A third region appears also somewhere between these 2 regions where the flow is not fully attached but not fully separated. This region is called as transitional region and, as it was stated in a previous chapter, commercial CFD software are not able to predict it. For the fully attached and the fully separated region, the drag coefficient seems to be unaffected from a certain Reynolds number and over. As it was mentioned earlier, the validation will take place for the fully separated and the fully attached region. The reason for this decision will be discussed later in the next chapter.

A radius ratio of 10% of Cooper's bluff body was chosen for the validation of the fully attached region. The geometry along with the computational domain are shown in the following images.

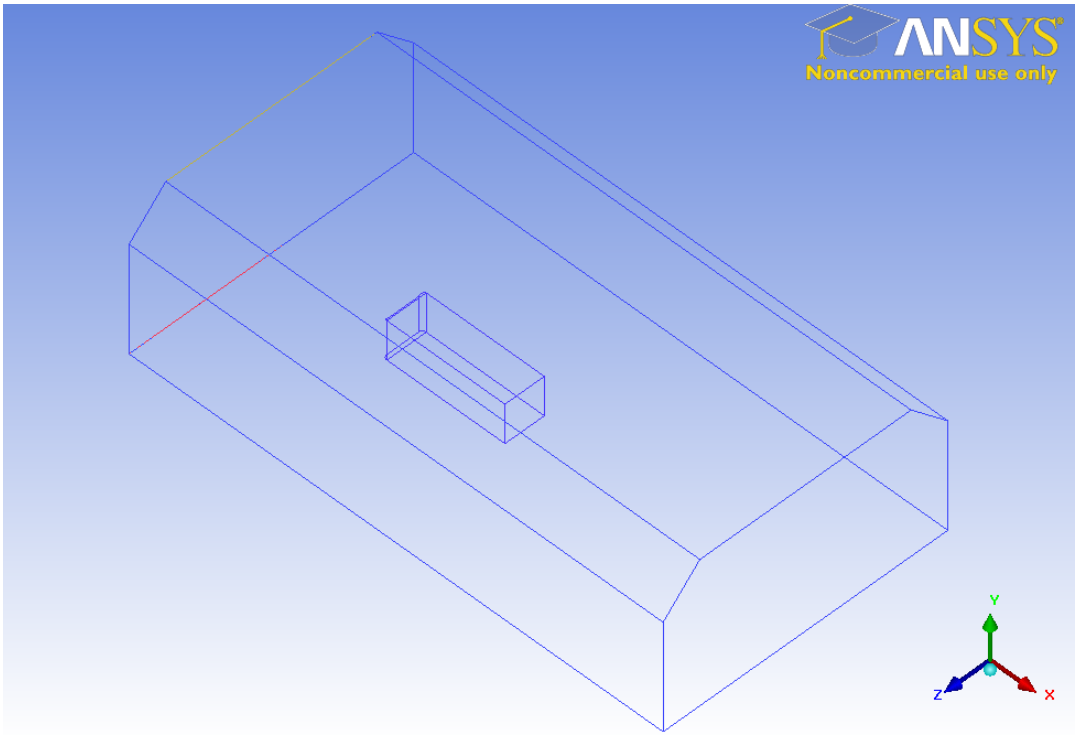

Figure 4.3: Cooper's bluff body and wind tunnel from a 3D point of view.

4.2 Fully attached flow

From a CFD perspective, the inlet region and the wake region should be extended because it is of vital importance that the flow should be fully developed when the air reaches the bluff body, as well as in the wake region. As a result, A computational domain with extended inlet and wake region was selected. This computational domain is represented in the following image with its numerical grid.

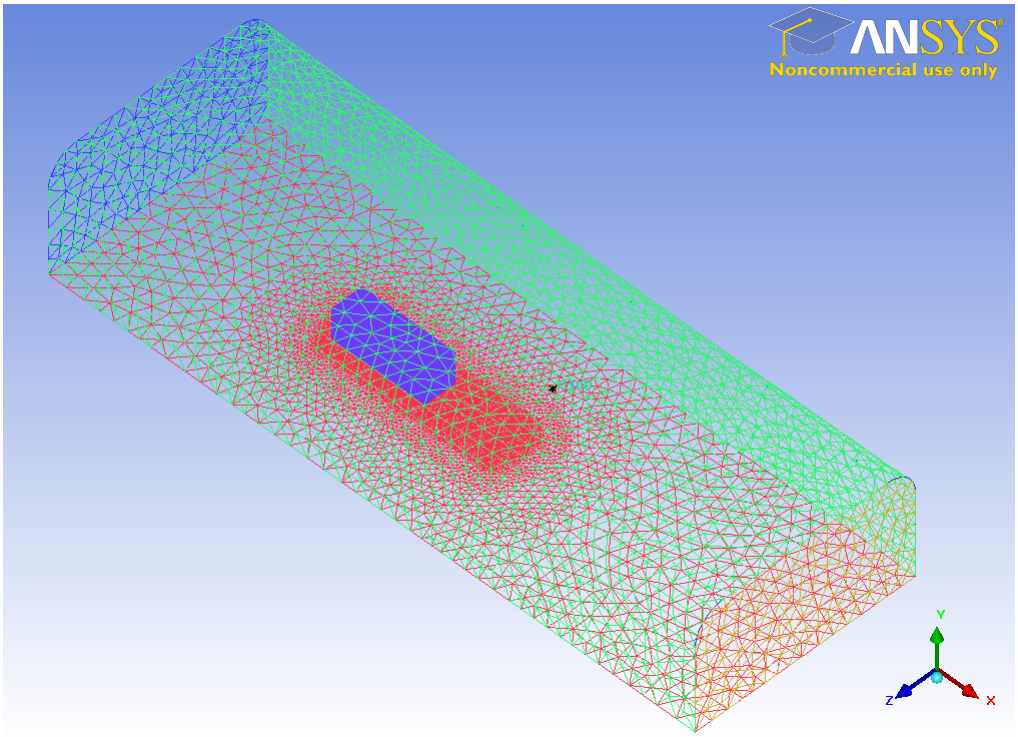

Figure 4.4: The computational domain that was used for the validation of Cooper's results.

In particular, the inlet region was extended to $2.1L$ and the wake region was extended to $4L$ where L is the length of the bluff body. It may seem contradictory that on the one hand the actual experiment must be validated numerically which means that the originally dimensions must be implemented, but on the other hand an extension of the inlet and wake region take place. The reason for these extensions is that numerical simulations, especially steady state simulations, cannot predict the development of the flow, that is the actual velocity profile. Consequently, an extension of the physical domain must be done, in order to enable the numerical solver to make the flow developed, like in the physical domain. Another change that was made in the computational domain, as it can be seen by comparing the 2 images above, was with the sharp edges at the left and right side close to the roof, where they were substituted with rounded edges. The reason for this change is again for numerical issues. Sometimes, sharp edges may cause problems in the iterative process of numerical simulations and may lead to instability and divergence. The next figure shows a closer look on the numerical grid from a 2D point of view.

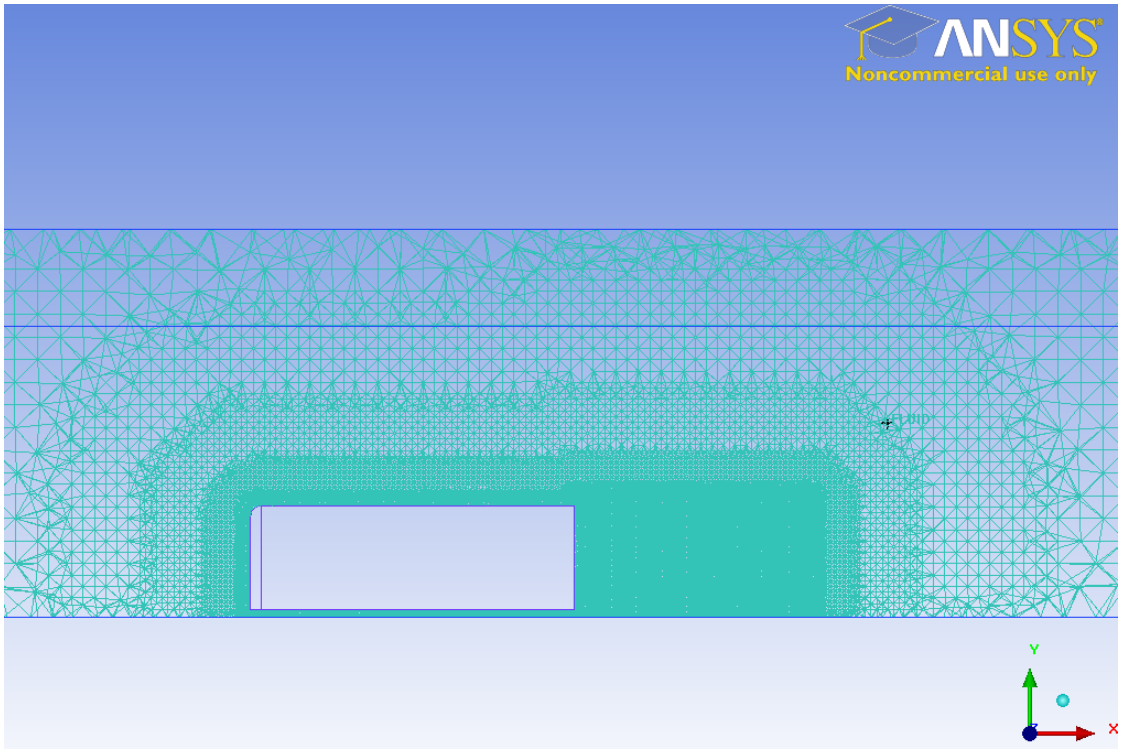

Figure 4.5: The numerical grid from a 2D point of view.

The density box has the same width and height as the blunt body and approximately 70% of the body's length. An expansion ratio of 1.2 was used in order to make the change smoother from the regions where the grid is very refined to the farfield where the grid is very coarse. The importance of this expansion ratio will be highlighted for the simulations of the bluff body with no roundings where the flow is fully separated. The worst quality of the grid is 30% which is considered as a good quality for unstructured grids.

Despite the fact that Cooper investigated the bluff body for a Reynolds number up to $2.5 \cdot 10^6$ approximately, the validation of his results is held for $Re = 3 \cdot 10^6$. The reasons for this selection are that the drag coefficient does not seem to change from a certain Reynolds number and over for all regions as it can be seen from figure 4.2, and the flow around the optimized geometries that are discussed later in this chapter are simulated for approximately $Re = 5.3 \cdot 10^6$ which is highly turbulent, so it would be wiser to select a Reynolds number closer to this value. A Reynolds number of $3 \cdot 10^6$ corresponds to a farfield velocity of approximately $115^{m}/_{s}$, because the characteristic length as it was defined in equation (4.1) is $D = 0.3809m$, which corresponds to a Mach number of 0.34 so compressibility effects cannot be neglected and a compressible solver must be used. Given the fact that compressible solvers are much more time consuming because a Riemann solver must be implemented, it was decided to scale up the physical domain by a

factor of 2, in order to reduce the velocity magnitude by the same factor, in such a way that the dynamic similarity is kept. The new characteristic length of the scaled up geometry is $D = 0.7618m$. As a result, the new Mach number is approximately $Ma = 0.17$ so an incompressible solver can be trusted. However, it should be kept in mind that this is the farfield velocity. The velocity close to the body is higher, especially close to the roundings because acceleration of the molecules take place, but it never exceeds the limit of $Ma = 0.3$. For $Ma = 0.3$, an error of approximately 5% is expected when an incompressible solver is implemented. Another simplification was that the mountings of the body were neglected, but given to their small size, the expected error is negligible. They seem like wheels but actually they are some kind of mountings which helped the bluff body to "suspend" and they were connected to some measuring devices. Cooper also measured the turbulence intensity at the inlet, a compulsory variable in order to fully specify the inlet boundary condition, and he found it 0.5%.

The settings of the simulations and numerical grid characteristics are presented below:

- Unstructured numerical grid consisting of 5,7100,000 tetrahedra
- Non dimensionalized distance from the walls $y^+ \approx 12$
- Steady state
- Pressure based solver
- Velocity inlet boundary condition for $57.5^{\mathrm{m}}/_{\mathrm{s}}$ which corresponds to $Re = 3 \cdot 10^6$
- Turbulence intensity 0.5% at inlet
- Length scale $0.027m$ at inlet
- Pressure outlet boundary condition at the outlet
- No slip boundary conditions for the rest boundaries
- 3^{rd} order MUSCL scheme for the momentum equation
- 1^{st} order scheme for turbulence models

The rest features in the software were left as their default values.

The following table makes a comparison of various turbulence models for Cooper's model for a radius ratio of 10% where the flow is fully attached for $Re \approx 1.3 \cdot 10^6$ and over.

Turbulence model	Drag Coefficient
Standard $k-\varepsilon$	0.39
Standard $k-\omega$	0.413
Spalart Allmaras	0.389
$k-\omega$ SST	0.318
$k-\varepsilon$ Realizable	0.314
$k-\varepsilon$ RNG	No convergence

Table 4.2: Parametric study of turbulence models for the validation of Cooper's results.

In the following diagram a comparison of a digitized version of Cooper's diagram for radius ratio 10% with numerical results of various turbulence models is conducted.

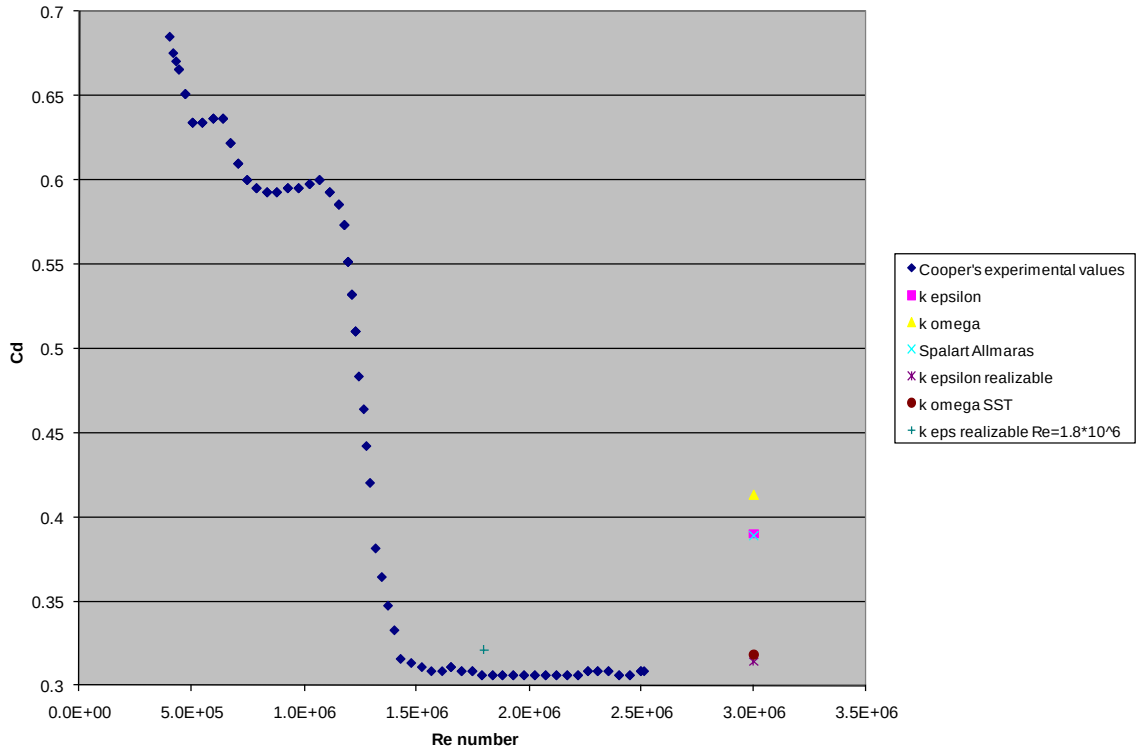

Figure 4.6: Comparative diagram of Cooper's results for radius ratio 10% with numerical results for various turbulence models.

As it seems from figure 4.5, as well as from the original diagram of Cooper's results, figure 4.2, the value of drag coefficient does not change significantly from $Re \approx 1.4 \cdot 10^6$ up to $Re \approx 2.5 \cdot 10^6$, that is the fully attached region, so it is expected to have the same value for $Re = 3 \cdot 10^6$. The digitization of Cooper's diagram exports a drag coefficient of $C_D \approx 0.308$ for this range of Reynolds numbers. Consequently, the most favorable

turbulence models for this application are the k - ω SST and the realizable k - ε. The difference of these models as well as their deviation from the experimental value for the drag coefficient is almost negligible, considering also the error of the digitization of Cooper's diagram. However, the realizable k - ε model was chosen as the most appropriate model, and this model was implemented throughout this dissertation. The reasons for this selection are because the realizable k - ε performed slightly better that the k - ω SST, and also the latter could not converge when simulated a bluff body with no radius ratio where the flow is fully separated. This will be shown later in this project. Finally, as far the the convergence behavior is concerned, the following table represents the convergence of each equation for both models:

Equations	Realizable	SST
Continuity equation	$1.2 \cdot 10^{-4}$	10^{-5}
x momentum equation	$1.1 \cdot 10^{-6}$	$5.2 \cdot 10^{-6}$
y momentum equation	$6.4 \cdot 10^{-7}$	$3 \cdot 10^{-6}$
z momentum equation	$6.7 \cdot 10^{-7}$	$3.2 \cdot 10^{-6}$
1^{st} equation of turbulence model	$1.3 \cdot 10^{-5}$	$4.4 \cdot 10^{-5}$
2^{nd} equation of turbulence model	$1.1 \cdot 10^{-5}$	$1.3 \cdot 10^{-5}$

Table 4.3: Residuals of each equation for k - ω SST and realizable k - ε turbulence models.

The residuals of each equation were fluctuated around the values stated in the table above. The 1^{st} equation of turbulence model stands for the equation of turbulence kinetic energy for both models. while the 2^{nd} equation of turbulence model stands for the eddy dissipation for the realizable k - ε model and the specific dissipation rate for the k - ω SST model. In general, simulations with these residuals are not to be trusted without any other clue of confidence because they did not achieve the limit of 10^{-5} which is considered as the highest limit that a simulation should reach in order to be trusted [7]. As a result, both simulations were left to run for around 10,000 iterations which is a considerable amount of iterations in order to reach a stable drag coefficient value. Fortunately, a steady drag coefficient value was achieved for all models within less that 10,000 iterations so, the results can be trusted. Finally, the drag coefficient value was $C_D = 0.318$ for a second order discretization scheme for the momentum equation. The third order MUSCL scheme slightly improved the results, so this is the scheme that will be applied in the next simulations in the present thesis.

The next figures illustrate the y^+ distribution around the Cooper's model from a 2D and 3D point of view.

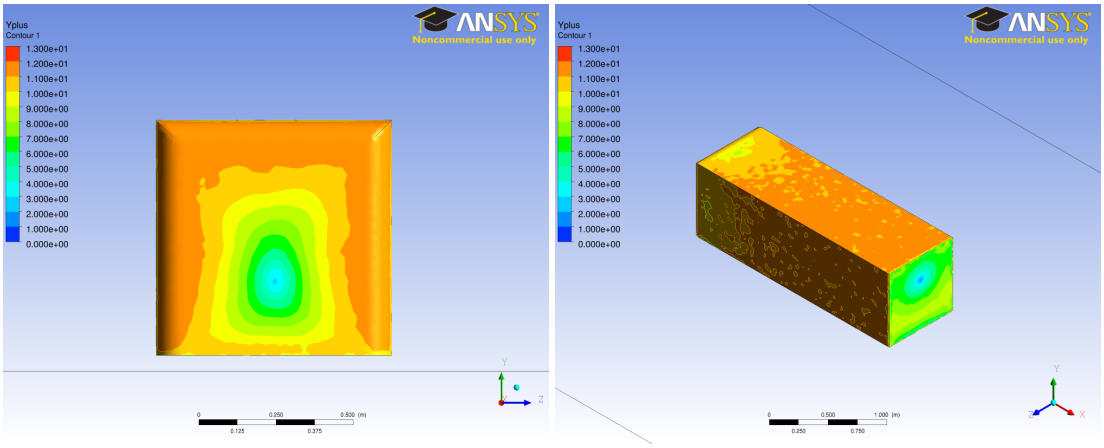

Figure 4.7: 2D and 3D point of view of the y^+ value respectively around Cooper's model.

It can be easily observed from the images above, that the y^+ value never exceeds the limit of 12. It appears to have lower values in the frontal area and at the rear of the body because the velocity of air at these regions becomes smaller. The point where appears that the y^+ value is almost zero is the stagnation point where the total pressure has its highest value. The next 2 figures illustrate the pressure coefficient value around the body.

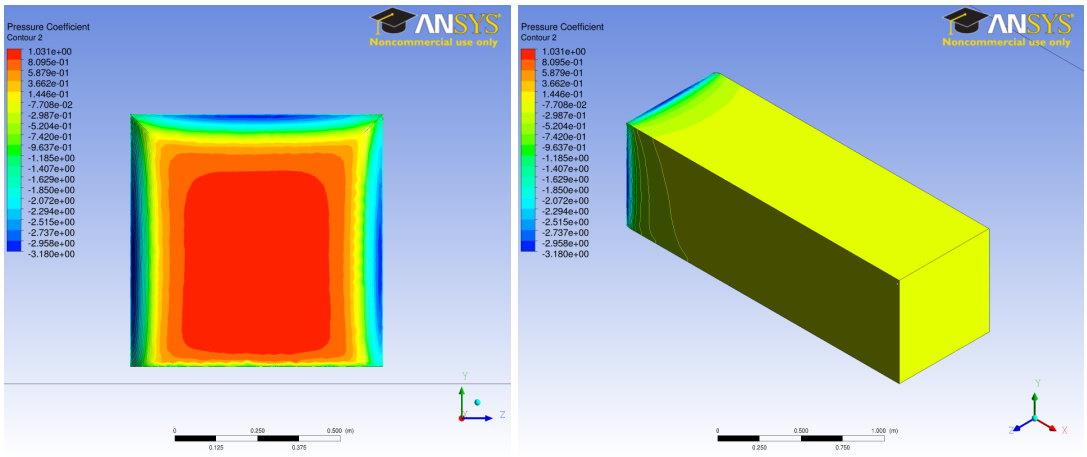

Figure 4.8: Pressure coefficient distribution around the body from a 2D and 3D point of view.

The pressure coefficient seems to have its lowest value at the roundings which makes total sense because the velocity is accelerated at these regions, so keeping in mind the energy conservation law, the pressure drops. The negative values of pressure coefficient is due to the fact that the static pressure at these regions is smaller that the reference pressure. Ideally, for an isentropic flow, the pressure coefficient should be equal to 1. However, in nature there are no isentropic flows because there is always friction between

the molecules, so the pressure coefficient should be smaller than 1. However, as it is observed from the contour maps above, it seems that the pressure coefficient exceeds the limit of this value, so the results seem to be non realistic. The overprediction of pressure coefficient is a common issue with RANS modeling. It has to do probably with the interpolation of the values that the software uses. Another possible explanation is that it is an error by the turbulence model. Many turbulence models sometimes overpredict the turbulent kinetic energy, so this lead can lead to slightly non realistic results. Since the pressure coefficient does not exceed the limit of 1 very much and the drag coefficient is well predicted when compared with experimental data it can be trusted. In the rest regions it appears to have a stable value.

The following images show the streamline distribution around the body.

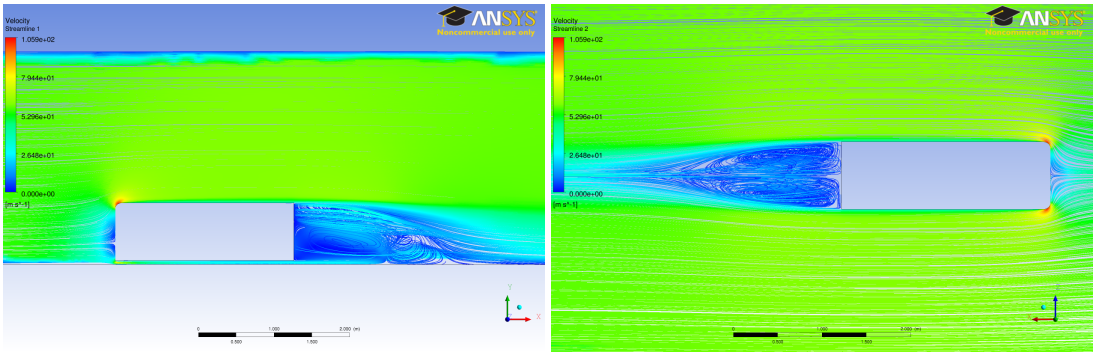

Figure 4.9: Streamline distribution around the body from 2 different angles.

As it was assumed and stated many times earlier, the flow is fully attached everywhere around the body. The region at the frontal area where the velocity has low values can be observed, and this is the region where the pressure coefficient has its highest values. The velocity accelerates close to the rounded edges and has its highest value. It appears from these images that the maximum velocity magnitude appears to be$105.9 \mathrm{m/s}$. This velocity corresponds to $Ma = 0.311$. Since it slightly exceeds the limit of $Ma = 0.3$ which is the threshold in order to use a compressible solver and also given the fact that these regions are very small in relation to the rest domain, the assumption of the usage of an incompressible solver was correct. Finally, at the rear of the body, the region where strong vortices occur can be observed, which is the main source of the drag coefficient. This statement will be proven in the next chapter.

In order to verify to a great extent the validity of the turbulence model realizable k - ε, a simulation for $Re = 1.8 \cdot 10^6$ is performed. For this specific Reynolds number, a lower velocity magnitude is required, so the height of the first prism layer must be modified. In order to avoid this procedure, the domain is scaled up by a factor of 1.2 instead of 2, like in the case of $Re = 3 \cdot 10^6$. Consequently, the grid settings and the

velocity inlet remain exactly the same. The only necessary changes that are applied is the frontal area of the truck and the length scale at the inlet boundary condition. The frontal area for this case is $A = 0.20881m^2$ and the length scale is $l = 0.032m$, because the new characteristic length of the model becomes $D = 0.45708m$. The exported value of the drag coefficient is $C_D = 0.321$ as it seems in figure 4.5 while the real value should be again $C_D \approx 0.308$. This value makes an error of around 4.2% which is higher than the case of $Re = 3 \cdot 10^6$. One possible explanation for this deviation of drag coefficient between these 2 different Reynolds numbers may lie to the fact that turbulence models perform better in highly turbulent flows. In general, the higher the Reynolds number, the more reliable the results are. This happens because in low Reynolds numbers the flow may be not fully turbulent but turbulence models are not supposed to model transitional regions or laminar flows. On the other hand, a flow with a Reynolds number of $1.8 \cdot 10^6$ is fully turbulent so, theoretically, it should perform as good as for the case of $Re = 3 \cdot 10^6$. However, an error of 4.2% in general is acceptable for CFD simulations. Finally, as it was stated earlier, the optimized geometries are simulated for $Re \approx 5.3 \cdot 10^6$, so theoretically, the expected error should be very small as in the case of $Re = 3 \cdot 10^6$.

4.3 Grid Independence

As it was stated earlier, an unstructured numerical grid consisting of $5.71 \cdot 10^6$ tetrahedra is used for the parametric study of various turbulence models for $y^+ \approx 12$. A numerical grid for Cooper's model with the same features and characteristics is also used for Cooper's model without the roundings of the frontal area, in order to validate also the case where the flow is fully separated. Of course, the selection for this grid size was far from random. The following table represents the GCI (Grid Convergence Index) values for various grid sizes. The variable which is considered is the drag coefficient. It should be stated here that size of the cells in the farfield region was stable. During the grid convergence study, the size of the cells around the body and the density box was changed.

Grid size	C_D	ε	GCI
$1.07 \cdot 10^6$	0.38	-	-
$2.11 \cdot 10^6$	0.341	0.1144	0.0172
$3.34 \cdot 10^6$	0.327	0.0428	0.0144
$7.87 \cdot 10^6$	0.309	0.0583	0.0048

Table 4.4: GCI values for the Cooper's model of 10% radius ratio.

ε stands for error which is given by the following formula:

$$\varepsilon = \frac{C_{D,i} - C_{D,i+1}}{C_{D,i+1}} \tag{4.3}$$

GCI is computed by the following relation:

$$GCI = \frac{\varepsilon}{\left(\frac{N_{i+1}}{N_i}\right)^n - 1} \tag{4.4}$$

N_i stands for the number of elements of the numerical grid and n stands for the order of the discretization scheme that was used. In this case, as it was stated earlier, the 3^{rd} order MUSCL scheme was used, so n is equal to 3.

It is clear from the table above that the GCI value always descends which means that the change of the examined value, that is the drag coefficient in this case, becomes smaller and smaller as the grid is refined. Strictly speaking, a more refined grid should be used until the GCI value starts to increase, which practically means that, in the best case, the grid of $7.87 \cdot 10^6$ would be used for the computations. However, instead of this, a grid consisting of $5.71 \cdot 10^6$ cells was selected for the validation process, as it was mentioned earlier. The selection of this grid size is due to the following reasons. First of all, since the GCI value is very small for the final grid, it is likely that a more refined grid would export a higher GCI value and the difference in drag coefficient would be negligible, so the grid consisting of $7.87 \cdot 10^6$ cells would be considered as the most practical for this application. Also, since experimental data are available, it is clear that the grid of $7.87 \cdot 10^6$ almost reached the experimental value of $C_D = 0.308$. Moreover, a grid consisting of 10 or 12 million cells, necessary for the grid convergence study, is not that practical, or even unfeasible to be created and simulated due to the limitations of the available hardware. Finally, this procedure was done for the validation of experimental data and it was successful with a small error with a grid of $5.71 \cdot 10^6$ cells. A more elaborated and proper grid convergence study will take place on the optimized geometries later. Since, a steady state simulation was sufficient in validating the experimental values of Cooper's experiments, there is no need to perform any transient simulation at least for this case.

4.4 Other parametric studies

So far, only one value for y^+ was examined, that is $y^+ \approx 12$. Also, a simplification of the original wind tunnel (the computational domain represents the wind tunnel) was

done by substituting the sharp edges which connect the roof and the sides of the tunnel, with rounded curves. Finally, the distances of $2.1L$ and $4L$ for the inlet and wake region respectively, may be questionable since in other similar studies, as well as in this thesis in the next chapter where the optimized geometries are simulated, authors tend to use extended inlet and wake regions. In this section, a parametric study for y^+, for the inlet and wake region, for a symmetry plane, as well as one simulation with the original wind tunnel used by Cooper, is examined.

The following images illustrate the prism layers around the rounded frontal area for $y^+ \approx 12$ and $y^+ \approx 30$ respectively. Since the height of the first layer is increased for the case of $y^+ \approx 30$, only 18 prism layers were used, instead of 25.

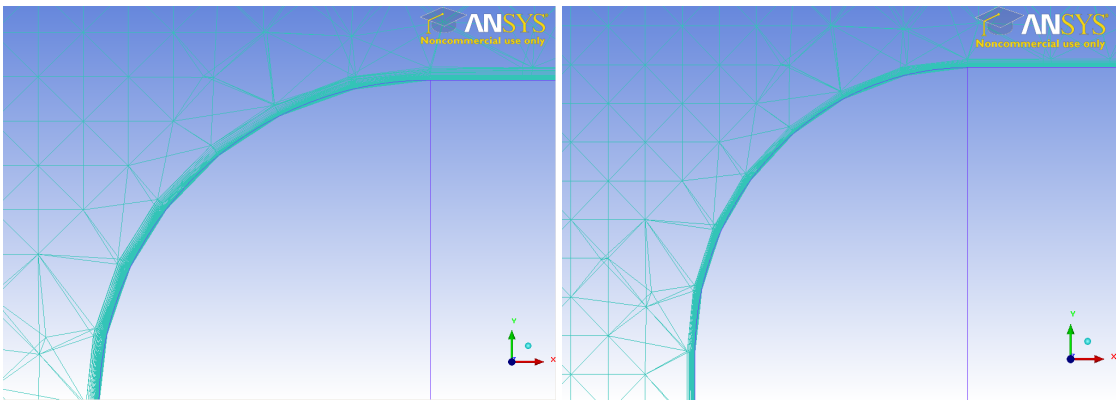

Figure 4.10: A 2D illustration of prism layers around the frontal rounded area for $y^+ \approx 12$ and $y^+ \approx 30$ respectively.

As seen in the figures above, the total height is in the same order of magnitude. In particular, the total height for the cases of $y^+ \approx 12$ and $y^+ \approx 30$ are $0.2304mm$ and $0.2475mm$ respectively. The computed drag coefficient with the grid of $y^+ \approx 30$ is $C_D = 0.331$ which makes a considerable relative error of 7.5%. The reason for this increment may be very complicated since it has to do with the wall functions applied by the software. Unfortunately, convergence with a grid of $y^+ \approx 1$ could not be achieved. Consequently, the value of $y^+ \approx 12$ is the optimum for this application.

The following image illustrates the computational domain that was used for Cooper's bluff body with frontal radius edge ratio of 10%. The same grid and flow settings were applied like in the stage of validation process. The only difference is at the dimensions of the inlet and wake region of the domain. Instead of $2.1L$ and $4L$ for the inlet and wake region respectively, an inlet region of $3L$ and a wake region of $6L$ is used.

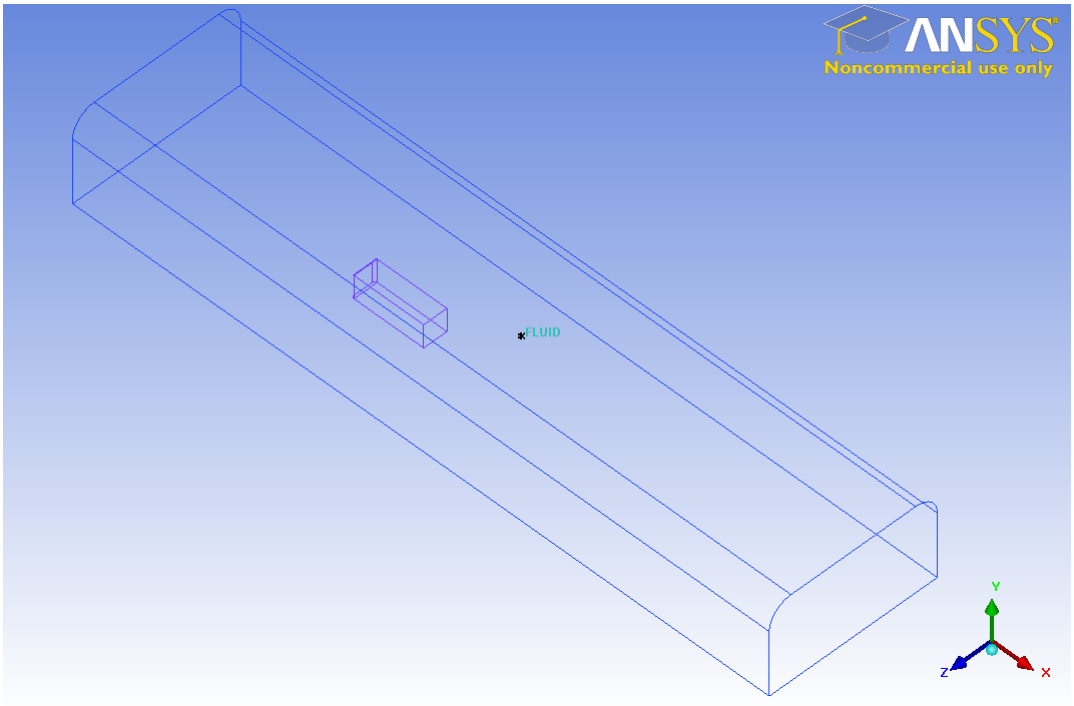

Figure 4.11: The computational domain with extended entry and wake regions.

The exported drag coefficient for this extended computational domain is $C_D = 0.317$ which is slightly worse in relation to exported value from the smaller domain. However, the difference between these 2 values is less than 1%, so in practical terms, the appropriate dimensions for the computational domain were chosen.

The following figure illustrates the computational domain without the roundings of the edges which connect the roof of the domain with the side walls.

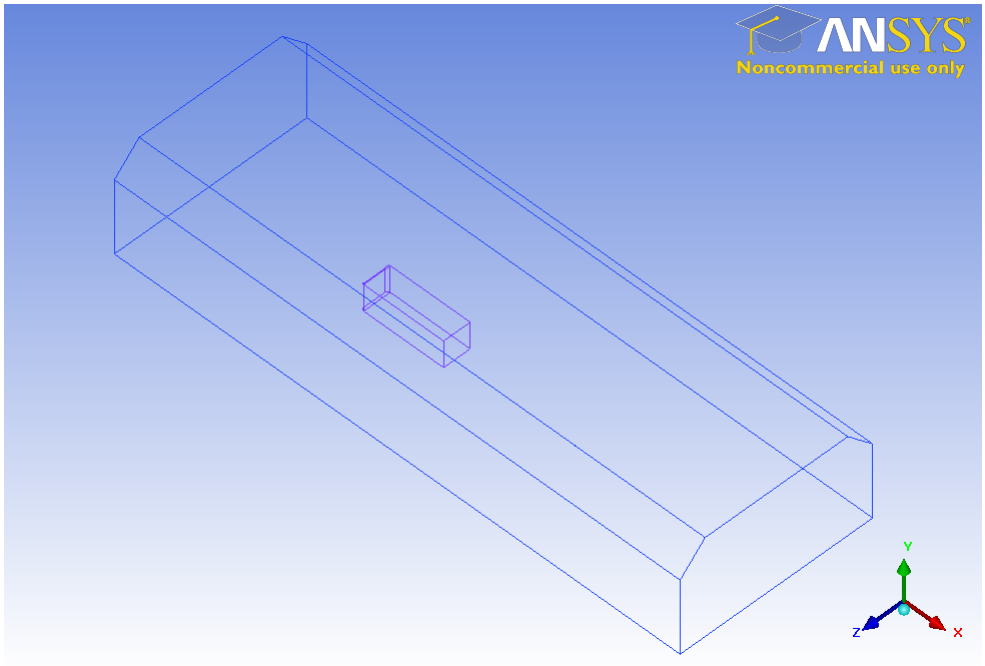

Figure 4.12: The computational domain with sharp edges like Cooper's original wind tunnel.

As in the previous cases, all the parameters and features of the grid and flow are the same. The computed drag coefficient is $C_D = 0.312$ which is practically the same as in the case of the domain with the rounded curves having a difference of 0.6%.

In many engineering applications, when the geometrical characteristics of the domain are symmetrical, it is a common practice to simulate only the half of the domain, and reflect the flow field at the other half of the domain which is not simulated, for post processing. This concept has the basic advantage of the decreased computational cost because only half of the required number of cells is required. However, it should be used after careful consideration because sometimes, even if the the domain is symmetrical, the flow field is not necessarily symmetrical, especially in turbulent flows. The following image illustrates the domain that was used for this application.

As in the previous case, the same flow characteristics were used, except for a symmetry boundary condition at the symmetry plane of the domain. Unfortunately, the exported drag coefficient was $C_D = 0.301$ which has a non negligible relative error of 4.1% from the simulation without the symmetry. This difference shows that the flow field is not symmetrical, consequently, it cannot be used throughout this project. This assumption could be made by a closer look at the figures 4.9. The strong vortices that occur seem to be slightly different in size.

4.5 Fully separated flow

Finally, the same settings regarding the numerical grid were applied for Cooper's bluff body without any roundings on the frontal area. Taking a closer look on Cooper's graph, it can be observed that bluff bodies with small values of leading edge radii ratios are characterized by high drag coefficients because the flow is fully separated. The drag coefficient values, like in the case of attached flows, they do not seem to be affected by the Reynolds number from a certain value of the latter and over. The computed drag coefficient value by the software of this case was $C_D = 0.942$. The following graph shows a digitized version of Cooper's experimental values for this case compared with the numerical value for $Re = 3 \cdot 10^6$.

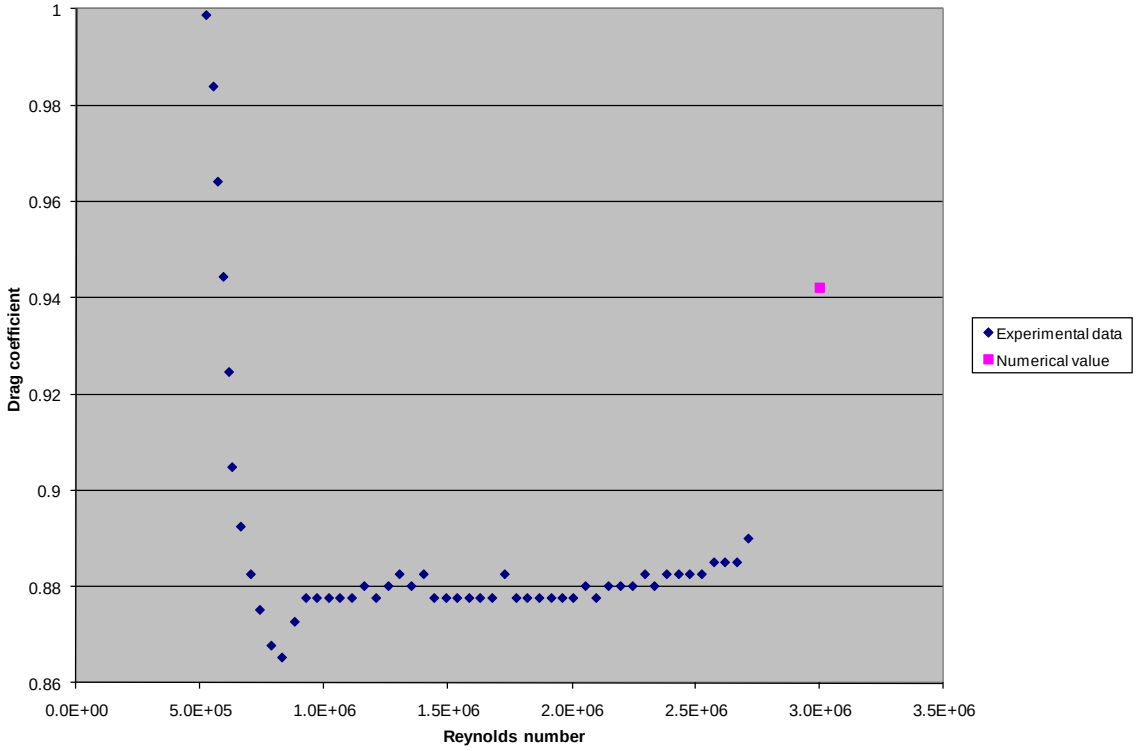

Figure 4.13: Comparative diagram of Cooper's results for no radius ratio with numerical results.

It can be observed that experimental values by Cooper are available for up to $Re = 2.7 \cdot 10^6$, while the numerical is for $Re = 3 \cdot 10^6$. It seems that, contrary to the attached case, here there is a slight increase of the drag coefficient with the Reynolds number. The drag coefficient for $Re = 2.7 \cdot 10^6$ is $C_D = 0.89$ according to Cooper's experiments. Assuming that this is the same value for $Re = 3 \cdot 10^6$, the relative error of the numerical value

is 5.8%. However, the error may be little smaller if the drag coefficient is little higher for $Re = 3 \cdot 10^6$. The error for the separated flow is higher in relation to the attached flow, nevertheless it can be considered as an acceptable error for CFD applications. Unfortunately, convergence with the model k - ω SST could not be achieved as the fluctuations of the drag coefficient value were random and non periodic. As a result, the realizable k - ε model is the only one to be trusted for the fully separated flow case despite its increased relative error compared to the attached case. The following images show the pressure coefficient distribution and the streamlines around the body.

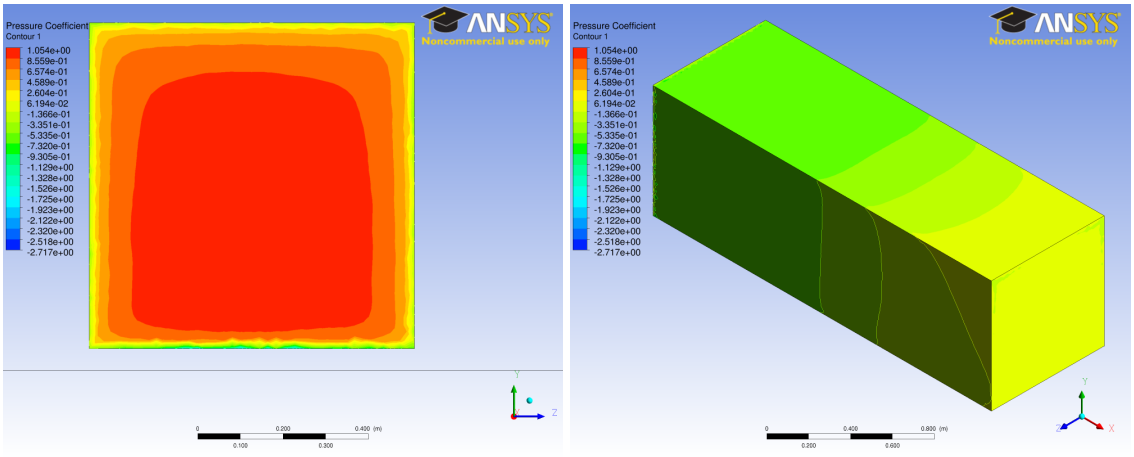

Figure 4.14: Pressure coefficient distribution around Cooper's body with no roundings at the leading edges.

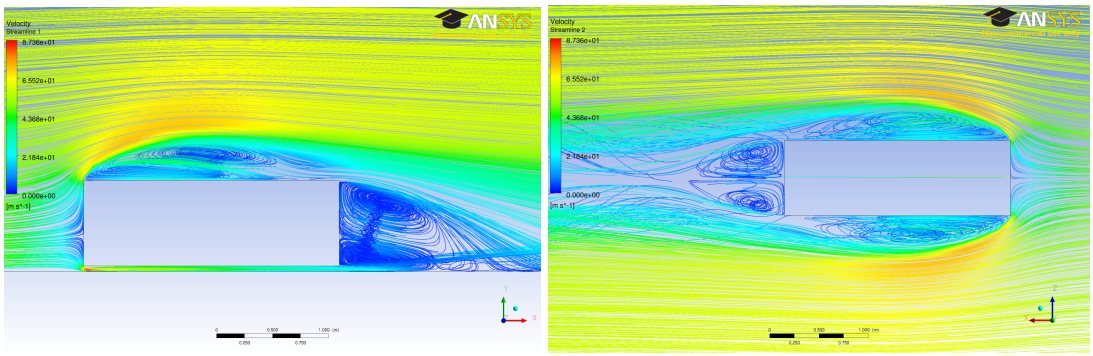

Figure 4.15: Streamlines around Cooper's blunt body with no roundings at the leading edges.

The pressure coefficient distribution is almost the same as for the fully attached flow case. The only difference is that it appears to have a slightly higher maximum pressure coefficient value. As far as the streamlines are concerned, it is clear that the flow is fully

separated and the reattachment point seems to be close to the rear of the body. These strong vortices are responsible for the high drag coefficient for this case despite the fact that the vortices at the rear seem to be smaller regarding to their magnitude and intensity.

4.6 10° yaw angle

In the nature, it is a very common phenomenon for the wind to blow in random directions and sometimes with high velocity magnitude, especially in north countries. Consequently, the case of a yaw angle of 0° is very rare. Depending on the direction and magnitude of the air, the yaw angle of trucks and other automobiles can exceed a yaw angle of 45°. In this section, an effort is put to validate Cooper's results for a yaw angle of 10°. The numerical grid and flow features remain the same. The only difference take place at the velocity inlet boundary condition. Instead of the absolute value of $57.5^{\mathrm{m}}/_{\mathrm{s}}$, the value of $57.5 \cdot \cos 10^\circ = 56.626^{\mathrm{m}}/_{\mathrm{s}}$ is input for the velocity in the x direction, and the value of $57.5 \cdot \sin 10^\circ = 9.985^{\mathrm{m}}/_{\mathrm{s}}$ is input for the y direction. The computed drag coefficient from the software was $C_D = 0.229$ which is far different from Cooper's experimental value. By taking a closer look on Cooper's graph the, drag coefficient for 10° yaw angle for 10% radius ratio for $Re > 1.8 \cdot 10^6$ seem to be approximately $C_D \approx 0.35$ making a relative error of 35%, so under no circumstances should the results be trusted. A final effort was put into validation of Cooper's results for the case of 10° yaw angle with a transient simulation. The same settings were applied also in this simulation. The time step was selected to be $\Delta t = 0.01s$. Since an implicit method is implemented by the software, there is no restriction for the Courant number. Consequently, any time step value can be selected. A sensitivity analysis can show the most appropriate time step selection, but this procedure is beyond the scope of this assignment and there was not much available time. The transient simulation was performed to check whether or not there was some improvement on the drag coefficient value. The simulation used as initial condition the results from the steady state simulation and was simulated 2 physical seconds. There was no point in simulating more physical time because the results did not change during the simulation. On the contrary the computed drag coefficient was exactly the same as in steady state simulation at the 3^{rd} decimal figure, that is $C_D = 0.229$. Therefore, the validation of Cooper's experiments completely failed for yaw angle of 10°, so no simulations for non zero yaw angles for the optimized geometries are performed.

Chapter 5

Optimized models

From the previous chapter enough confidence was gained through the validation process with experimental data of blunt bodies, especially for the case of the attached flows where the error was almost negligible. However, it should be stated that Cooper's experiments took place inside a wind tunnel while the optimized geometries are simulated in the free field like real trucks, because experimental data on blunt bodies in the free field are not available. However, since there are no significant changes in the flow, as well as in the geometries, the confidence that was gained can be preserved for free field flows.

The following images illustrate the blunt body that is investigated with the 3 different frontal shapes.

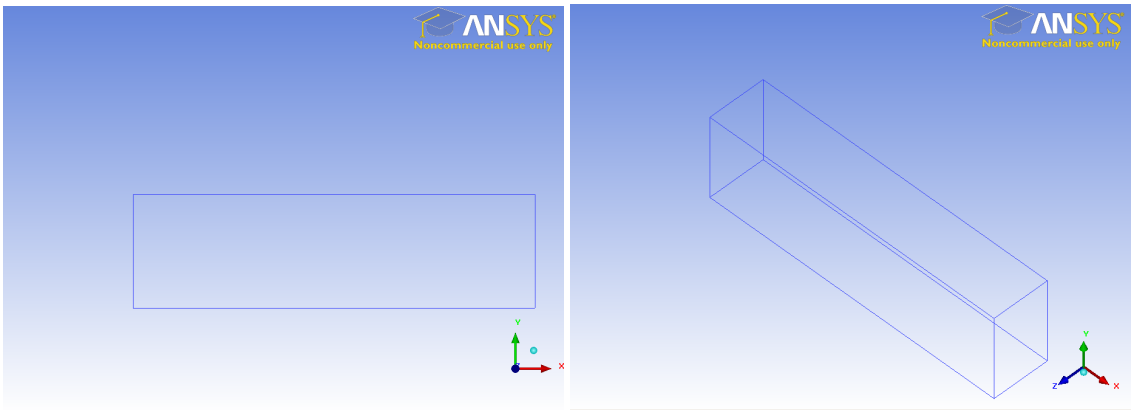

Figure 5.1: 2D and 3D points of view of the rectangular box (model 1).

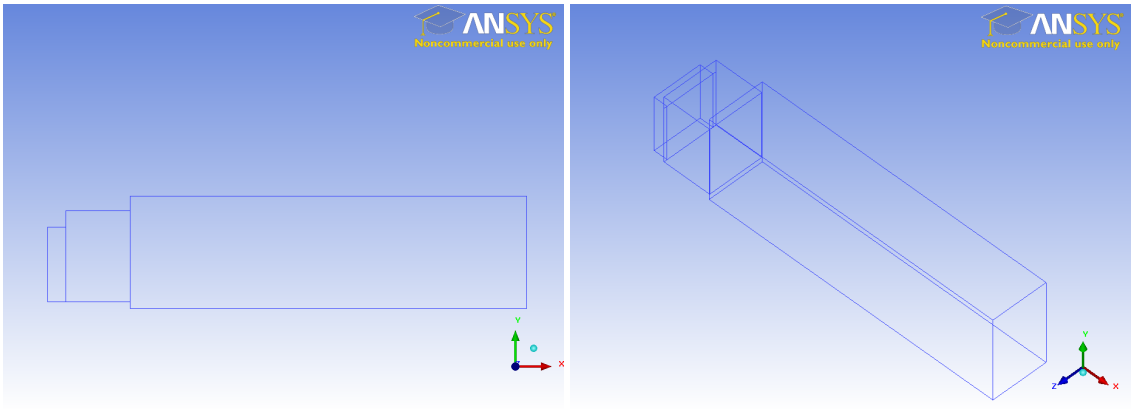

Figure 5.2: 2D and 3D points of view of model 2.

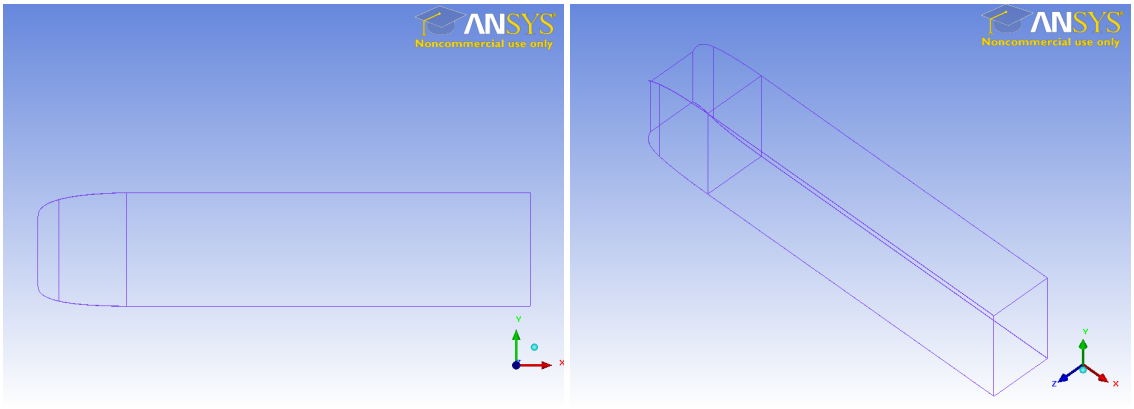

Figure 5.3: 2D and 3D points of view for the bluff body with the rounded frontal area (model 3).

The frontal area is the same for all of the geometries above since the bluff body has the same dimensions. The only difference is the front of it as it can be observed in the figures above. The dimensions of the rectangular box are summarized in the table below:

Length (m)	13.6
Width (m)	2.55
Height (m)	3.87
Ground clearance (m)	0.17
Characteristic length (m)	3.1414
Frontal area (m^2)	9.8685

Table 5.1: Dimensions of the rectangular box (model 1).

The characteristic length was computed according to Cooper's definition in the previous chapter. In almost all European countries, the maximum allowable speed limit for trucks is more or less $90^{\mathrm{km}/\mathrm{h}} = 25^{\mathrm{m}/\mathrm{s}}$. This velocity magnitude, for the characteristic length mentioned above, corresponds to $Re \approx 5.4 \cdot 10^6$, so the flow is highly turbulent. Lower velocity values are not considered throughout this project. The reason for this selection lies on the definition of the aerodynamic force. The aerodynamic force is defined as:

$$F_D = 0.5 C_D \rho A V^2 \tag{5.1}$$

From the relation above, it can be concluded that a reduction of velocity to 50% corresponds to a reduction of the aerodynamic force to 75%. Taking into account that, on the average, the aerodynamic force accounts for 40% to 60% approximately, depending on the operating conditions, of the total fuel consumption when the truck operates with a steady velocity $V = 25^{\mathrm{m}/\mathrm{s}}$, a reduction of the velocity to $V = 12.5^{\mathrm{m}/\mathrm{s}}$, when the rest parameters remain unchanged, the aerodynamic force accounts for only 10% of the total fuel consumption. This percentage is not negligible but even small amendments on the drag coefficient will have a very small impact on the fuel consumption of the truck. Also, the assumption of stable drag coefficient for this range of velocities is almost true because the velocity of $V = 12.5^{\mathrm{m}/\mathrm{s}}$ which is close to the upper limit of trucks inside residential areas, corresponds to $Re \approx 2.7 \cdot 10^6$, where the according to Cooper's diagrams in a previous chapter, the drag coefficient remains almost the same when the flow is either attached or separated. The flow starts to enter into the transitional region at lower Reynolds numbers. Taking all the above into consideration, it can be concluded that there is no point in spending valuable time for simulating lower velocity values.

The inlet and wake region of the optimized geometries is chosen to be $4L$ and $6L$ respectively, where L is the length of the body. This selection is not abrupt. The distance of the body from the inlet is significant because the flow must be developed before reaching the body, that is the reason it was extended to $4L$. As far as the wake region is concerned, the selection of $6L$ was based on the strong vortices that occur at the rear of the body which tend to decay after a long distance of the body. The height of the domain is $4.3H$ and its width is $3.5W$ at each side. The following figures show the blunt body with the computational domain with its numerical grid.

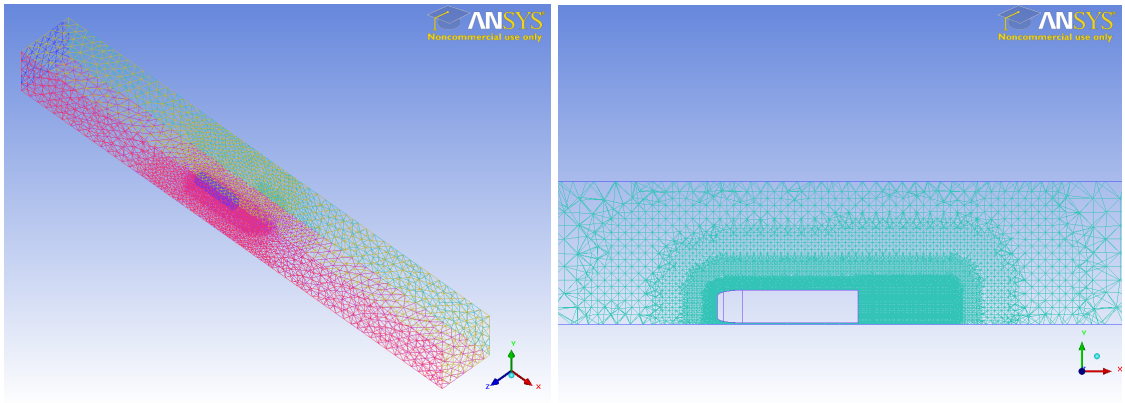

Figure 5.4: The computational domain with numerical grid of the bluff body with the rounded frontal area from a 3D and 2D point of view respectively.

In the figure above, the density box that was used can be observed. It has the same height and width with the bluff body and approximately 62% of the body's length. As in the validation stage of Cooper's results, a grid convergence study is proceeded here on the blunt body with the rounded frontal area. The spacing of the cells of the farfield were kept intact during the grid convergence study. During the study the variable was the spacing of the cells around the body as well as the the spacing of the density box. The The grid convergence study is based exclusively on the drag coefficient. It should be stated that the same parameters regarding the grid generation and flow field were applied here as in the validation of Cooper's results in the previous chapter. The only difference took place at the boundary conditions of the roof and the 2 perpendicular side walls of the domain. Instead of a no slip condition, a free slip boundary condition was applied since the body is supposed to be in the free field. The following table represents the computed CGI values.

Grid size	C_D	ε	GCI
$1.05 \cdot 10^6$	0.321	-	-
$2.08 \cdot 10^6$	0.284	0.037	$5.46 \cdot 10^{-3}$
$3.95 \cdot 10^6$	0.263	0.021	$3.59 \cdot 10^{-3}$
$7.71 \cdot 10^6$	0.244	0.017	$2.64 \cdot 10^{-3}$

Table 5.2: GCI values for the blunt body with the rounded frontal area.

The grid convergence study was successful as it can be observed from the table above since the GCI value decreases as the grid size increases. Instead of the time consuming grid size of $7.71 \cdot 10^6$ elements, a grid size of $6.25 \cdot 10^6$ elements is selected for the rest of the simulations. The computed drag coefficient from this grid size is $C_D = 0.246$ which is practically the same value computed by the very refined grid consisting of $7.71 \cdot 10^6$ cells. Consequently, this is the grid size that is applied for the rest simulations.

The following table represents the drag coefficient values for each optimized model for 0.5% and 5% turbulent intensity at the inlet. The flow settings are the same as in the validation stage. The only difference is that these are flows in the free field so, free slip boundary conditions were applied on the roof and at the perpendicular sides of the domain.

	0.5%	5%
Model 1	0.949	0.95
Model 2	0.519	0.526
Model 3	0.246	0.259

Table 5.3: Drag coefficients for the optimized models.

Turbulent intensity seems to play a minor role for model 1 and it seems to have a slightly more significant impact for model 3 with the rounded frontal area. However, in general, turbulent intensity does not change significantly the drag coefficient of the models. As it was expected, the lower drag coefficient is found for model 3 since it has a rounded frontal area. Model 2 seems to be the intermediate step between this model and the rectangular box. It should be stated here that an error of around 6% is expected for model 1 and an error of around 2% is expected for model 3. However, since the velocities here are smaller than in the validation stage, so the flow is more "incompressible" the expected error may be little decreased. Nevertheless, this difference should not be significant. These assumptions were made from the validation stage in the previous chapter as the realizable k - ε model seems to overestimate the drag coefficient. The next figures show the pressure coefficient distribution around the bodies.

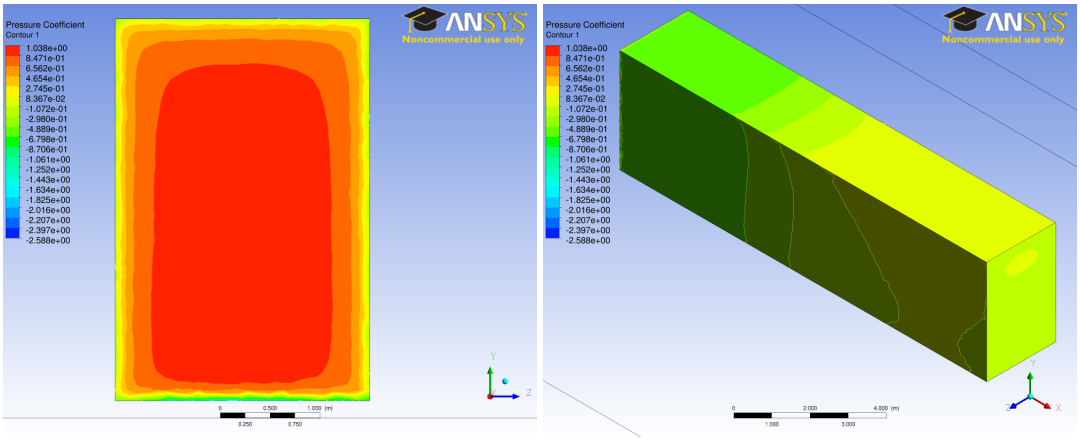

Figure 5.5: Pressure coefficient distribution around model 1.

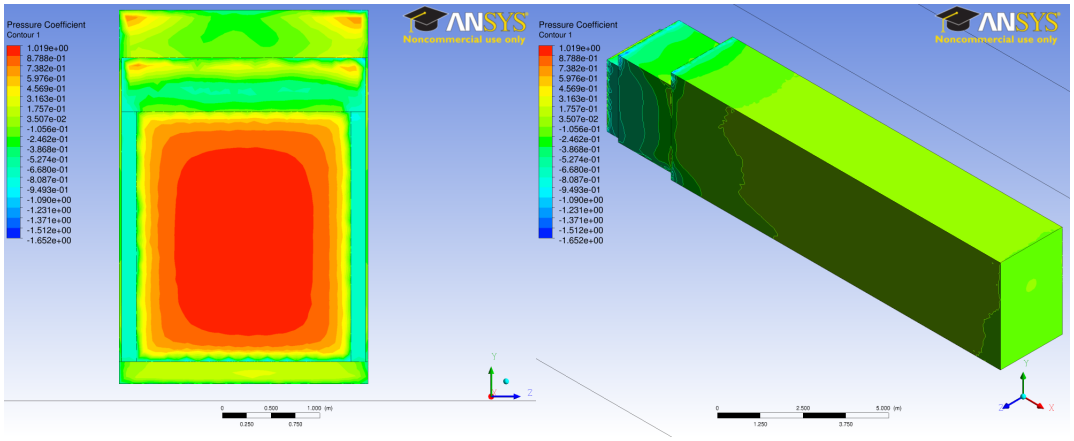

Figure 5.6: Pressure coefficient distribution around model 2.

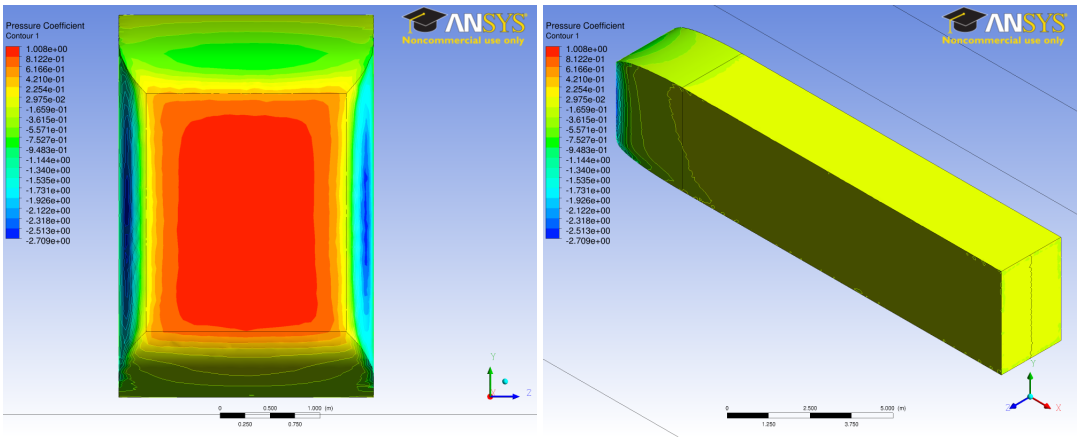

Figure 5.7: Pressure coefficient distribution around model 3.

The same assumptions can be made also here as in the validation of Cooper's models. The pressure drops at the roundings due to the acceleration of the velocity and the frontal area is the area that the pressure coefficient has its higher value. It is interesting again that the pressure coefficient exceeds the upper limit of 1.

The following images illustrate the streamlines around each of the models.

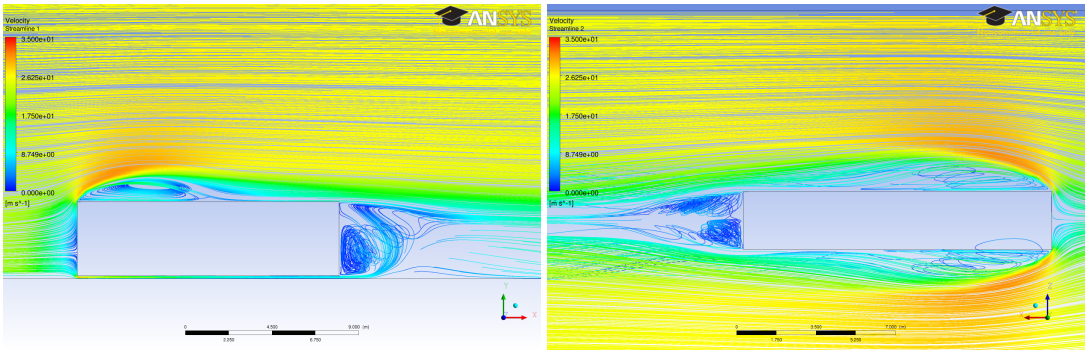

Figure 5.8: Streamline distribution around model 1.

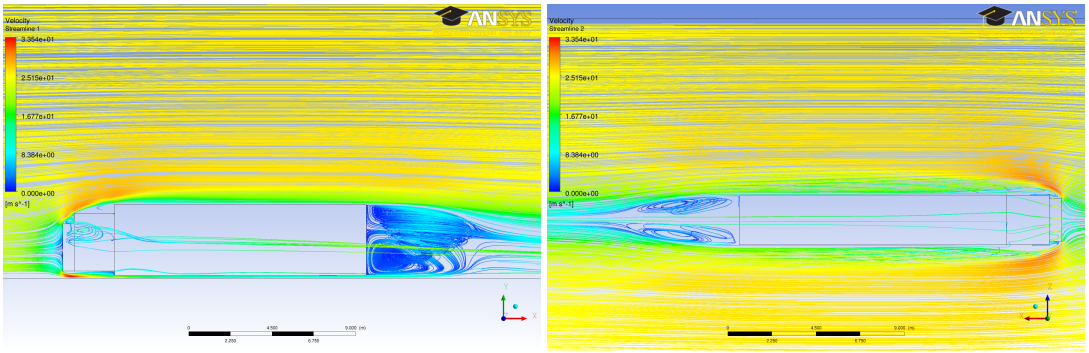

Figure 5.9: Streamline distribution around model 2.

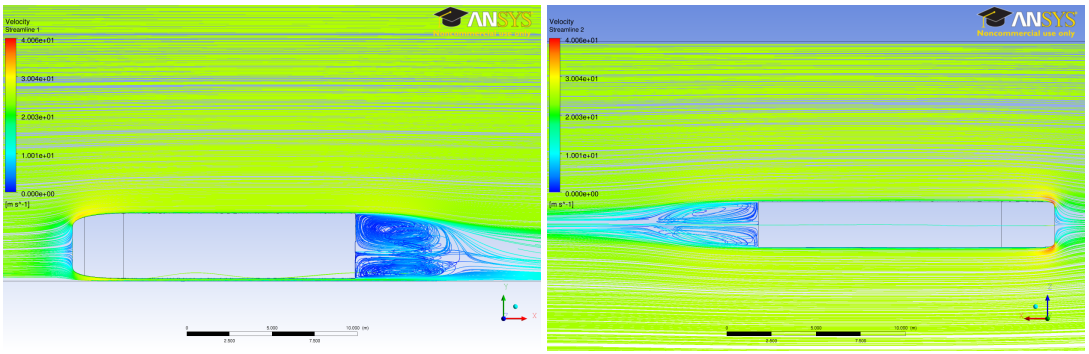

Figure 5.10: Streamline distribution around model 3.

The same trend of the streamlines is also visible here as in the validation chapter for models 1 and 2. The interesting part here is model 2 as it seems that the flow is almost attached at the roof of it and separated at the sides. However, these bubble region is not as intense as in model 1. It seems that at its frontal area some recirculations take place

but the flow seems to be attached. This is the reason why it appears to have a significant lower drag coefficient value in relation to model 1.

The following graphs show the balance between the drag coefficient introduced by pressure forces and the drag coefficient introduced my viscous forces for each model.

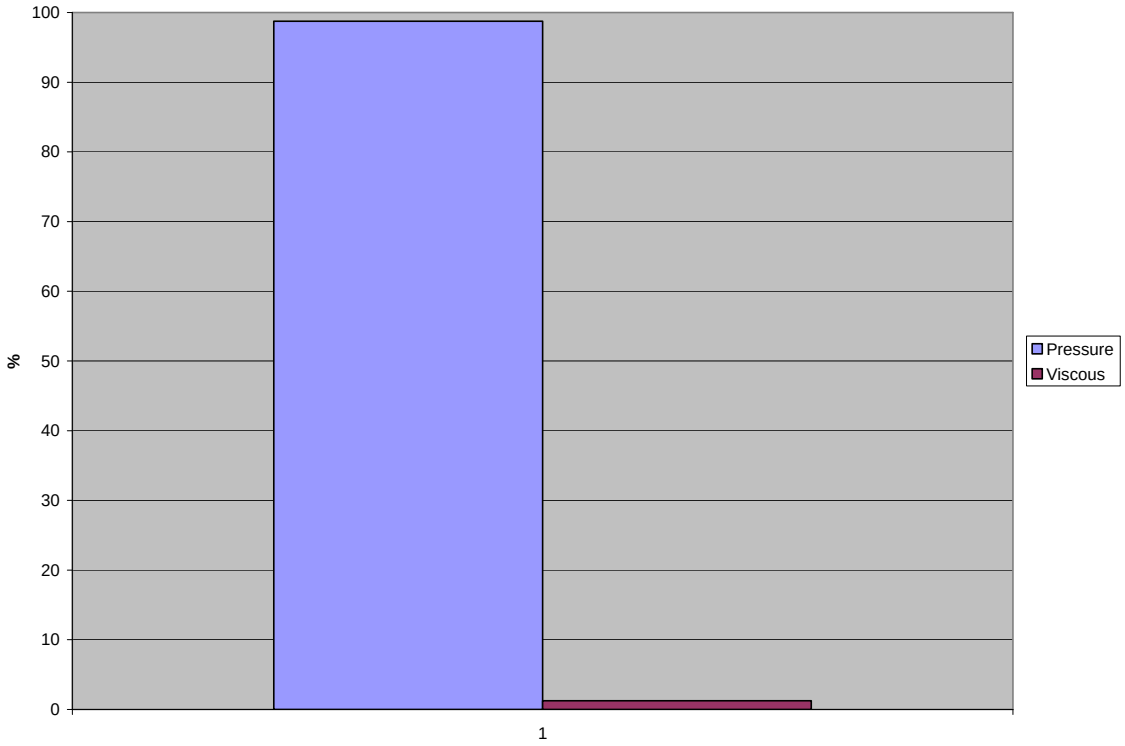

Figure 5.11: Balance between pressure coefficient from pressure forces and viscous forces for model 1.

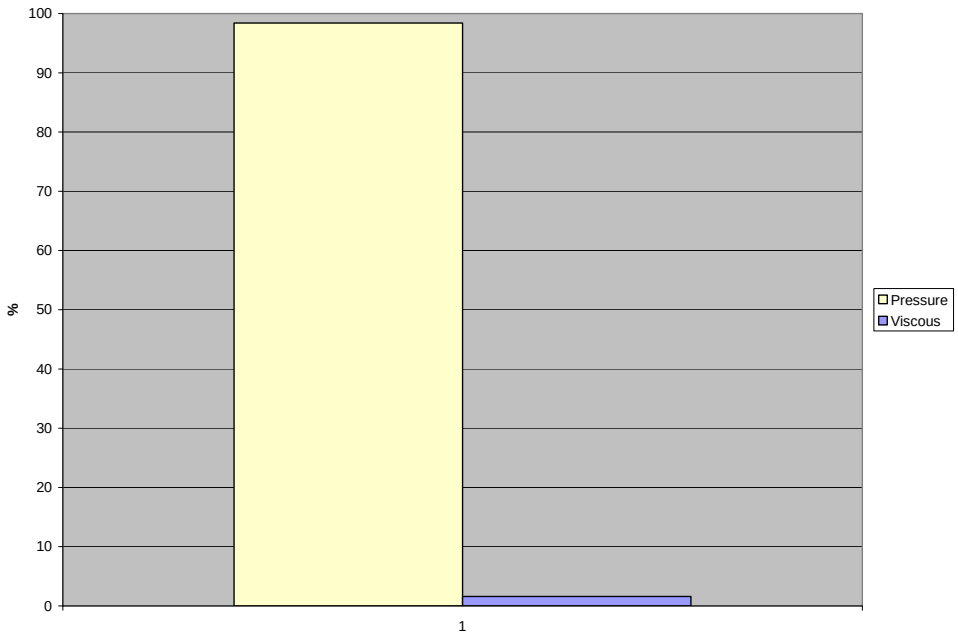

Figure 5.12: Balance between pressure coefficient from pressure forces and viscous forces for model 2.

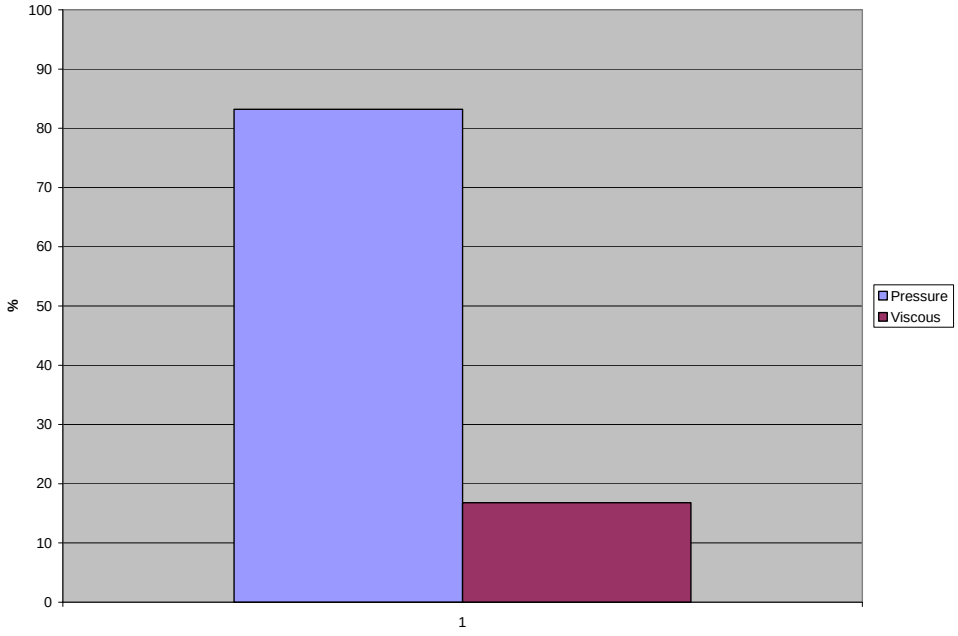

Figure 5.13: Balance between pressure coefficient from pressure forces and viscous forces for model 3.

It seems from the graphs above that for the first 2 models viscous forces play a negligible role to the total drag coefficient which makes total sense because they do not have any curves. On the contrary, in model 3, viscous forces start to become significant as they contribute to approximately 18% of the total drag. This fact deserves careful consideration since any dust of other kind of fouling may increase further not only the percentage of the viscous drag coefficient, but also the total drag of the vehicle. The next comparative graph shows the balance between the absolute values of pressure and viscous forces of the models.

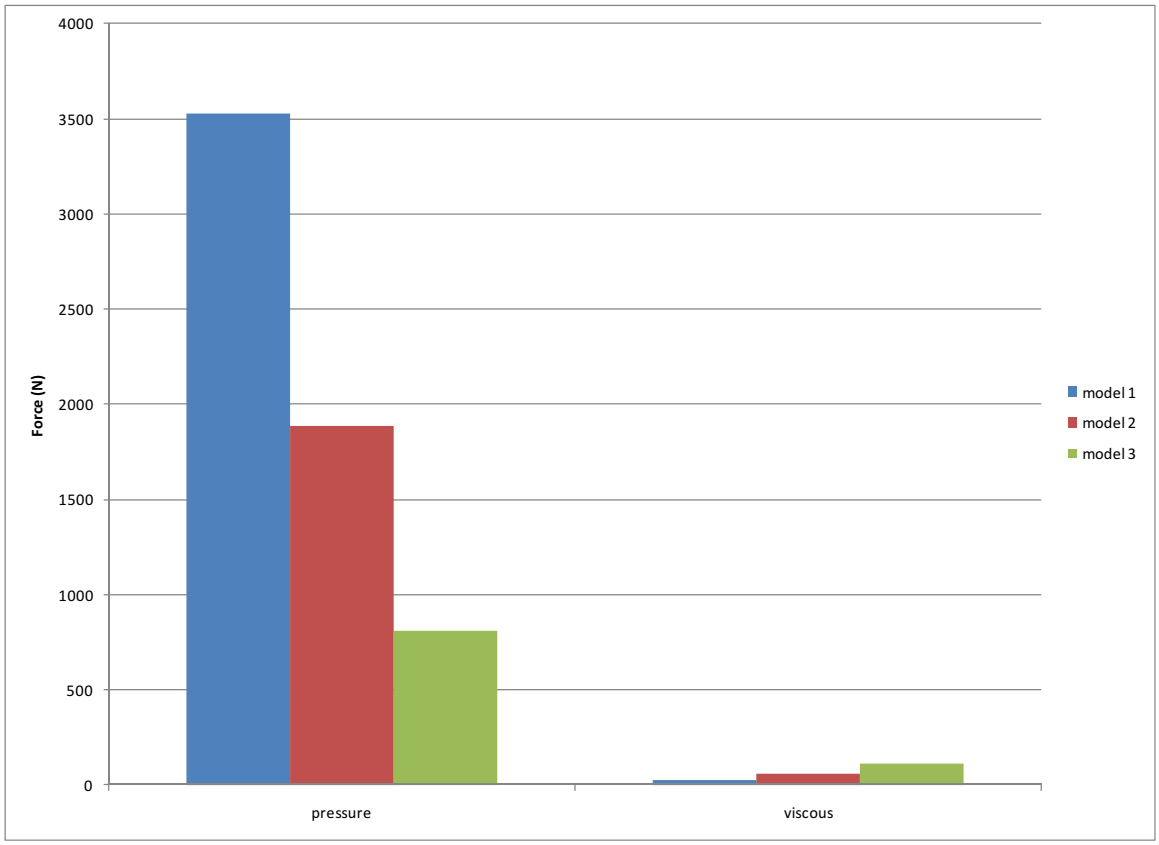

Figure 5.14: Comparison of pressure and viscous forces for all models.

A drop of pressure forces of approximately 75% for model 3 in relation to model 1 is clear with a slight increase in viscous forces. This is the explanation of the very low drag coefficient of this model.

In the next graphs the contribution of each part of the model, for all models, to the total drag coefficient is presented.

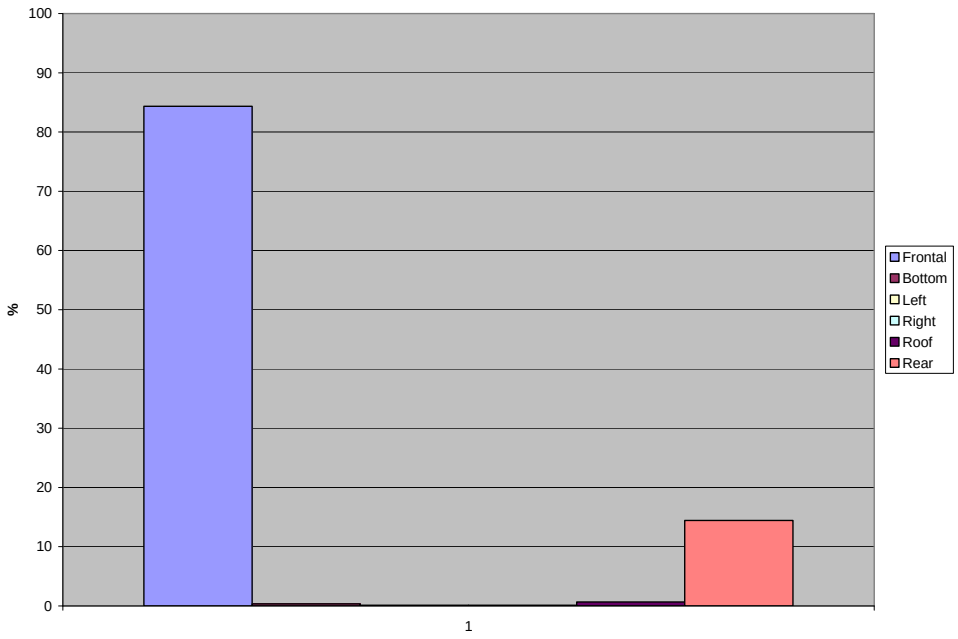

Figure 5.15: Contribution to the drag coefficient of each part of model 1.

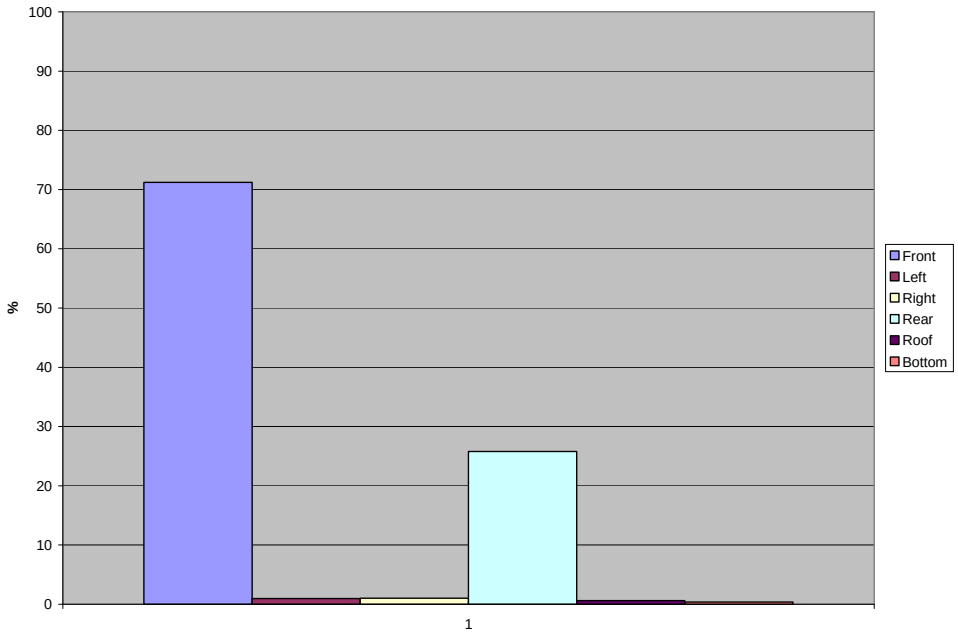

Figure 5.16: Contribution to the drag coefficient of each part of model 2.

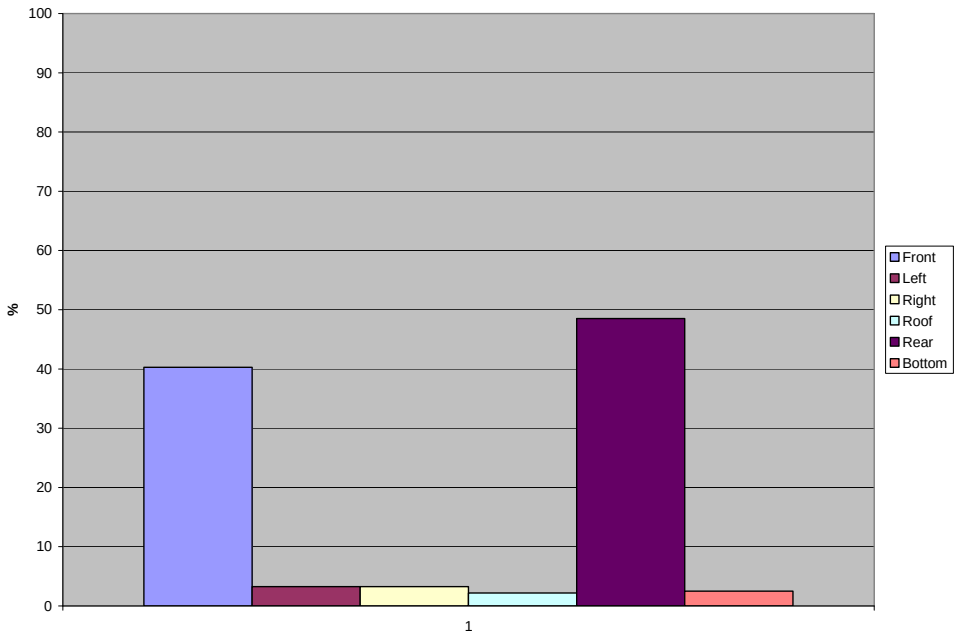

Figure 5.17: Contribution to the drag coefficient of each part of model 3.

For the first 2 models, it can be observed that the frontal part of them is mainly responsible for the drag coefficient which makes sense because this part the pressure forces are predominant. The second most important part is the rear due to their strong vortices of the air. In the third model, it seems that the rear of the truck contributes to the drag coefficient more than the front. This can be explained by the fact that the elliptical curves at the front reduce the drag coefficient to a great extent, but the rear of the body remains unchanged, so the same goes with the drag coefficient in absolute values but since the overall drag coefficient drops, its percentage to the drag coefficient increases. The rest parts, as it is expected, have a negligible contribution to the drag coefficient.

Chapter 6

Conclusions and Recommendations

Three different shape optimization models were simulated numerically and analyzed in this thesis project. These optimized models can very roughly represent trucks and their dimensions are close to them. After an introduction to the whole concept of the science of CFD and the numerical procedure that was followed, a validation process was held for Cooper's blunt bodies, since no experimental data were available for the optimized models. The validation process was successful for fully attached flows as well as fully separated flows for zero yaw angle with acceptable relative errors, so enough confidence was gained to simulate the optimized models. The validation of Cooper's experiments totally failed for a yaw angle of 10°, so simulations for this yaw angle were not performed for the optimized models. Pressure forces for all of the optimized models were predominant compared to viscous forces. The lowest drag coefficient was found for the model with a rounded frontal area since the flow is everywhere fully attached. Model 2, despite the fact that it does not have any roundings at any of its edge showed a promising improvement compared to the rectangular box. Even small roundings on its edges will decrease further the overall drag coefficient. However, it is the authors opinion that the drag coefficient of the simplified model will never drop below the one of the model with the rounded frontal area. The latter seems to have a very low drag coefficient, however, since viscous forces are significant on its frontal area, further improvements of it will lead to very small drops in the drag coefficient. Further improvements of this model can be attained by making the frontal area more elliptical with a very small frontal area normal to the flow or ideally with no frontal area normal to the flow, that is something like the frontal area of a bullet. Nevertheless, this shape is not practical for real trucks. Consequently, it is the authors opinion that an emphasis should be put into the rear of the truck where it contributes to a great extent into the total drag coefficient and given that it has sharp edges with no roundings, there is a lot of improvement that can be done.

Bibliography

[1] S. Patankar. *Numerical Heat Transfer and Fluid Flow*. CRC Press, New York, 1st edition, 1980.

[2] Filip Baillien. Cfd analyses of blunt body flows related to truck front shape optimization. *Msc Thesis*, Cranfield University:England, 2012.

[3] J.M.M. Luijten. Cfd study on gap effects of a simplified tractor semi-trailer model. *Msc Thesis*, Delft University:Netherlands, 2010.

[4] B. Hennemann. Modeling of front edge flow separation on rounded bluff bodies using commercial cfd software. Delft University:Netherlands, 2005.

[5] F. White. *Fluid Mechanics*. Mc Graw Hill, New York, 6th edition, 2008.

[6] D. Wilcox. *Turbulence Modeling for CFD*. DCW Industries, California, 3rd edition, 2010.

[7] Ansys products v.14 user's manual.

[8] H. Versteeg and W Malalasekera. *An introduction to Computational Fluid Dynamics. The Finite Volume Method*. Pearson, Essex, 2nd edition, 2007.

[9] Personal discussion with dr. laszlo konozsy.

[10] K. R. Cooper. Bluff body aerodynamics as applied to vehicles. *Wind Engineering and industrial aerodynamics*, 49:1–22, 1993.

[11] Kevin R. Cooper. Effect of front-edge rounding and rear-edge shaping on the aerodynamic drag of bluff vehicles in ground proximity. *In SAE Technical Paper Series*, 1985.